

A&A manuscript no. (will be inserted by hand later)
Your thesaurus codes are: 11(03.13.2; 11.05.2; 13.09.1)

ISOCAM observations of the Hubble Deep Field reduced with the PRETI method.*

H. Aussel, C.J Cesarsky, D. Elbaz, and J.L. Starck

Service d'Astrophysique, DSM/DAPNIA/CEA-Saclay, F-91191 Gif-sur-Yvette Cedex, France

Received 10 March 1998 / Accepted 25 August 1998

Abstract. We have developed a new ISOCAM data reduction technique based on wavelet analysis, especially designed for the detection of faint sources in mid-infrared surveys. This method, the Pattern REcognition Technique for Isocam data (PRETI) has been used to reduce the observations of the Hubble Deep Field (HDF) and flanking fields with ISOCAM at 6.75 (LW2) and 15 μm (LW3) Rowan-Robinson et al. (1997). Simulations of ISOCAM data allow us to test the photometric accuracy and completeness of the reduction. According to these simulations, the PRETI source list is 95% complete in the 15 μm band at 200 μJy and in the 6.75 μm band at 65 μJy , using detection thresholds which minimize the number of false detections. We detect 49 objects in the ISO-HDF at high confidence secure level, 42 in the LW3 filter, 3 in the LW2 filter, and 4 in both filters. An additional, less secure, list of 100 sources is presented, of which 89 are detected at 15 μm only, 7 at 6.75 μm only and 4 in both filters. All ISO-HDF objects detected in the HDF itself have optical or infrared counterparts, except for one from the additional list. All except one of the radio sources detected in the field by Fomalont et al. (1997) are detected with ISOCAM. Using a precise correction for the field of view distortion of ISOCAM allows us to separate blended sources. This, together with the fact that PRETI allows to correct data on the tail of cosmic rays glitches, lead us to produce deeper source lists than previous authors. Our list of bright sources agree with those of Désert et al. (1998) in both filters, and with those of Goldschmidt et al. (1997) in the LW3 filter, with systematic difference in photometry. Number counts derived from our results show an excess by a factor of 10 with respect to the prediction of a no evolution model (Franceschini 1998) in the LW3 band. On the contrary, the number of sources in the LW2 band is compatible with the prediction of such a model, but with

greater uncertainties, given the small number of detections.

Key words: Data analysis ; galaxies : evolution ; infrared : galaxies

1. Introduction

The observation with the Hubble Space Telescope (HST) of the Hubble Deep Field (HDF) (Williams et al. 1996) has yielded numerous new results in observational cosmology. This is due to its depth and spatial resolution in the near-UV and optical, allowing the computation of photometric redshifts of the observed galaxies as well as the determination of their morphological type. With the ground-based follow-up observations, in the near IR (Hogg et al. 1997a, Connolly et al 1997) for example, or at radio wavelength (Fomalont et al. 1997), as well as spectroscopic measurements (Steidel et al. 1996, Cohen et al. 1996), this field now constitutes a very important database for the study of galaxy formation and evolution. Among the striking results that have been already produced (see Ellis (1997) for a review), two have strong implications on the galaxy formation picture. First, the star formation rate (SFR) at high redshifts has been derived (Madau et al. 1996), and together with that computed from Canada France Redshifts Survey (CFRS) data at lower redshifts (Lilly et al. 1996), it seems to indicate that the bulk of star formation arose below $z \sim 2$. Second, an increase of faint irregular galaxy counts around $z \approx 1$ has been reported (Abraham et al. 1996), as well as the lack of detection of quiescent evolving early types galaxies at high redshifts. These results tend to favor the hierarchical galaxy formation picture.

However, the interpretation of these results is now being widely discussed. For instance, it has already been pointed out that the fainter objects seen in the HDF could merely be star forming regions of galaxies and not entire galaxies, because the distance between detected objects is small with respect to the size of a galaxy (Colley et al. 1996). This idea is supported by new simulations that

Send offprint requests to: H. Aussel

* Based on observations with the Infrared Space Observatory (ISO). ISO is an ESA project with instruments funded by ESA Member States (especially the PI countries : France, Germany, The Netherlands and the United Kingdom) and with participation of ISAS and NASA.

Correspondence to: aussel@discovery.saclay.cea.fr

show that diffuse emission from evolved stellar populations is below the detection limit of the HDF, while star forming regions with high UV surface brightness can be detected (Hibbard & Vacca 1997). For similar reasons, quiescent evolving early-type galaxies at redshift of $z \sim 3$ are also undetectable (Maoz 1996).

Most of the data that were used to derive star formation rates are UV and optical data from the CFRS and the HST itself, which are sensitive to extinction. Indeed, it has been shown that star formation at high redshift is obscured, typically by ~ 2 to 3 mag at $\lambda = 1620\text{\AA}$ (Meurer et al. 1997). The SFR inferred might therefore change if the reprocessing of UV by dust into IR is taken into account. Knowledge of the dust content of galaxies is therefore relevant to assess the results obtained so far, both at $z < 1$ with the CFRS and at higher redshifts. Additional information on this problem can be obtained by observing the HDF field in the infrared.

Many models have been built to compute the infrared spectra of various types of galaxies (AGN, starbursts, early types, *etc*) and make predictions on the number counts for surveys in the infrared (see, for example, Franceschini et al. (1991)). Moreover, various groups have derived new IRAS 60 μm counts, going to the extreme limits of the sensitivity of this satellite. Their results show an excess of sources with respect to the predictions of a scenario with only passive luminosity evolution of galaxies (Bertin et al. 1997, Gregorich et al. 1995). However, the exact amount of evolution needed is still a matter of debate, because the number counts derived by the various teams are slightly different. This issue needs to be revisited on deeper samples. From this point of view, the HDF field is a great opportunity to test these models, first because their number count predictions can be checked against observations, and second because all the information at other wavelengths is of great help to test the hypotheses of the various models.

Since the HDF field is rather small ($\sim 5 \text{ arcmin}^2$) and very deep, infrared observations require a good spatial resolution as well as a good sensitivity. This can be achieved by the mid-IR imager ISOCAM of the Infrared Space Observatory (ISO) (Kessler et al. 1996), which has proven to be 1000 times more sensitive than IRAS, with a 50 times finer spatial resolution (Cesarsky et al. 1996). Part of the Director's Time was dedicated to complete these observations, at 6.75 μm and 15 μm , for a total amount of 12.5 hours, with M. Rowan-Robinson as Principal Investigator (Serjeant et al. cite Serjeant, Goldschmidt et al. 1997, Oliver et al. 1997, Mann et al. 1997, Rowan-Robinson et al. 1997). The data of the ISO-HDF are now in the public domain, and we present here the results of our processing.

The ISOCAM observation of the HDF, hereafter ISO-HDF, is at the moment the deepest survey obtained in the 15 μm band. It is also deep in the 6.75 μm band, although a deeper integration on the Lockman Hole was obtained by Taniguchi et al. (1997) with this filter. We have

developed a new technique for ISOCAM data reduction, based on wavelet analysis (Starck et al. 1998) : the Pattern REcognition Technique for ISOCAM data (PRETI). Compared to data that we have at hand from less deep surveys in the Lockman Hole, from the Guaranteed Time program by Cesarsky et al. (1996), and in the shallow survey of the ELAIS program, this set has a much higher redundancy, and thus is useful for finding the ultimate capacities of our data reduction method. In addition, since the ISO-HDF has been analyzed by other teams such as Rowan-Robinson et al. (1997) and Désert et al. (1998), this observation allows us to compare the results from our method to those of more classical ones. All these methods aim at extracting very faint sources in ISOCAM data, and independent reduction techniques improve the quality of the produced catalogs. In section 2, the characteristics of the emission expected from galaxies in the MIR are outlined, and compared to the bandpasses of the ISOCAM filters that were used for the HDF observation. In section 3 we present the data acquisition and stress the critical steps of the reduction process. The way in which these difficulties are handled by the PRETI method is described in section 4. The efficiency of the method for source detection and its photometric accuracy was also tested on simulated data, which are presented in a section 5. Finally, we give our source catalog and number counts, compare them with those of other groups, and discuss the results. A more detailed interpretation of the results, source by source, will be presented in a forthcoming paper (Elbaz et al., *in prep.*).

2. MIR emission in ISOCAM filters

The ISO observations were performed in two broad band filters, LW2 (from 5.0 μm to 8.5 μm) and LW3 (from 12.0 μm to 18.0 μm). Figures 1 and 2 present synthetic spectra of the mid IR emission of galactic components between 1 and 20 μm . Figure 1 is a spectrum of a starburst galaxy, taken from Moorwood et al. (1996) for the 1 to 5 μm part and from Tran(1998) for the 5 to 18 μm part. Unidentified infrared bands (UIB) and ionization lines of Neon are clearly visible, as well as a hot dust continuum and silicate absorption. In this case, the derived temperature for the hot dust is about 200 K, using the model from Désert et al. (1990), and the extinction due to dust is about 3 mag, representative of a starburst region in a galaxy. The dotted line is a spectrum dominated by very hot dust heated at 1000 K, that could be typical of the mid-IR emission in the central core of an AGN, as observed by Aussel et al. (1998). Figure 2 depicts emission dominated by old population stars as modeled by Bressan et al. (1998), and is thus relevant for early-types galaxies.

The mid-IR (hereafter MIR) colours of galaxies are not simple, because the observed emission of a galaxy is a mixture of all the components shown on Fig. 1 and Fig. 2. According to the type of the object (early-type, AGN,

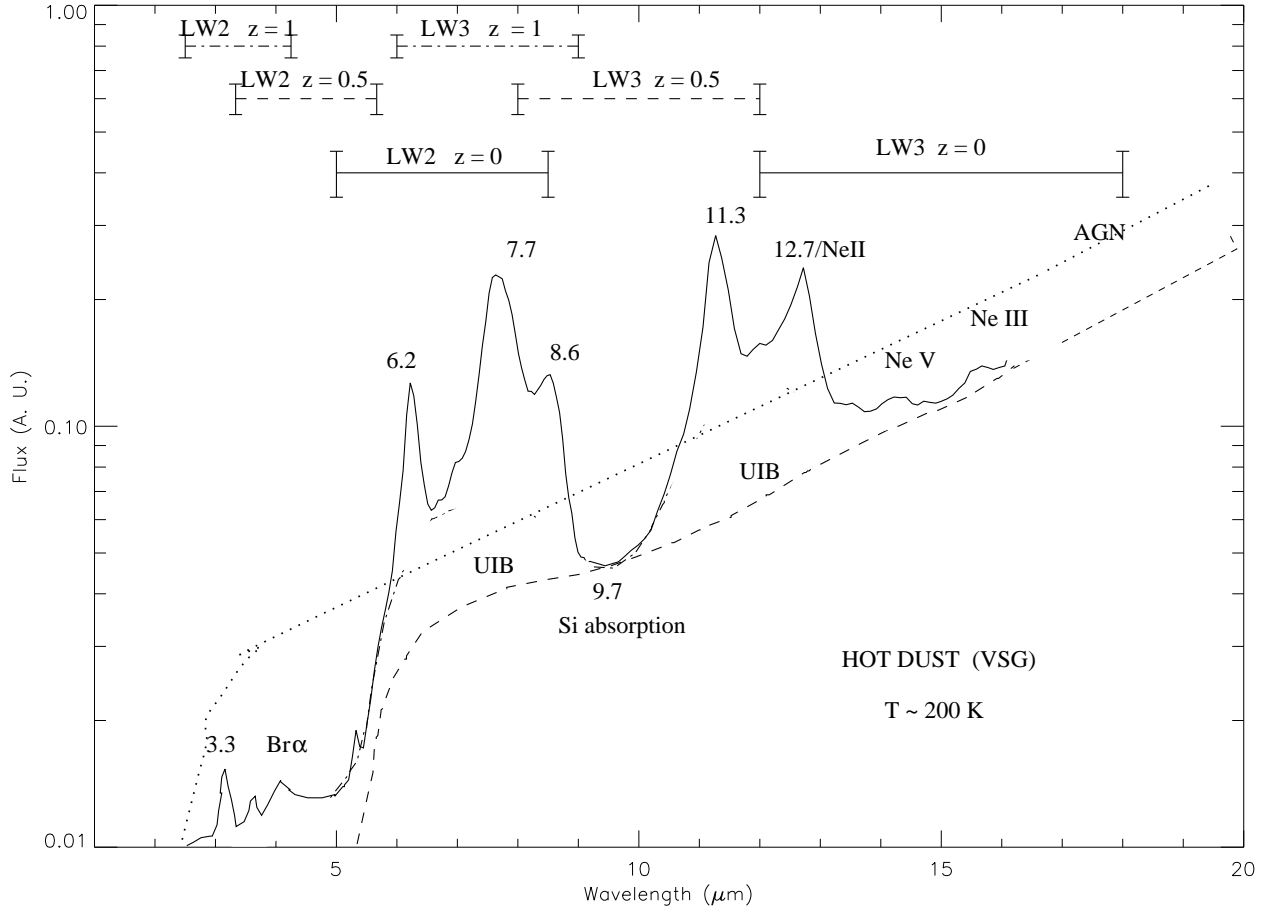


Fig. 1. Sketch of the mid IR emission of a starburst galaxy (after an original sketch of A. Jones) and of an AGN, compared with ISOCAM LW2 and LW3 filters bandpasses at various redshifts.

Solid line: total MIR emission of a starburst galaxy. The $5\mu\text{m} - 18\mu\text{m}$ part is an ISOCAM CVF observation showing all the typical UIB bands and ionization lines (spectra kindly provided by D. Tran). The $2\mu\text{m} - 5\mu\text{m}$ part was taken from a SWS spectrum of the Circinus galaxy (Moorwood et al. 1996), and scaled to the CVF spectrum.

Dashed line: contribution to the MIR emission of the hot dust. This dust is constituted of very small grains (VSG) (Désert et al. 1990) heated to a few hundred degrees.

Dotted-dashed line: Possible contribution of a continuum associated to the carriers of UIB.

Dotted line: Hot dust (1000 K) MIR emission of an AGN central part, as observed by Aussel et al. (1998).

starburst or normal galaxy), it is expected that a given type of emission will dominate (*e.g.* stellar, very hot dust or UIB). This is not always the case, as shown by Madden et al. (1998) on a sample of elliptical galaxies: most exhibit stellar colours in the MIR but some present MIR spectral energy distributions (SED) typical of UIB emission. Thus, the relative fluxes in figs. 1 and 2 are not to be compared directly.

In the rest frame, the LW2 filter is dominated by UIB features while the emission in the LW3 filter is due to the hot dust continuum, ionization lines of neon and the $12.7\mu\text{m}$ UIB plus the associated continuum. This picture changes dramatically when the redshift rises toward $z=1$:

the contribution of the stellar continuum, especially from old population stars, overtakes UIB features in the LW2 band, which in turn are shifted to the LW3 band, together with the silicate absorption band at $9.7\mu\text{m}$. The wavelength coverage for both filters is shown on both Fig. 1 and Fig. 2 for redshifts of 0, 0.5, and 1. This clearly indicates that the mid-IR observations can only be interpreted with the help of data at other wavelengths to disentangle the various contributions. This is possible on the HDF field, because UV, optical and near IR, as well as radio observations are available.

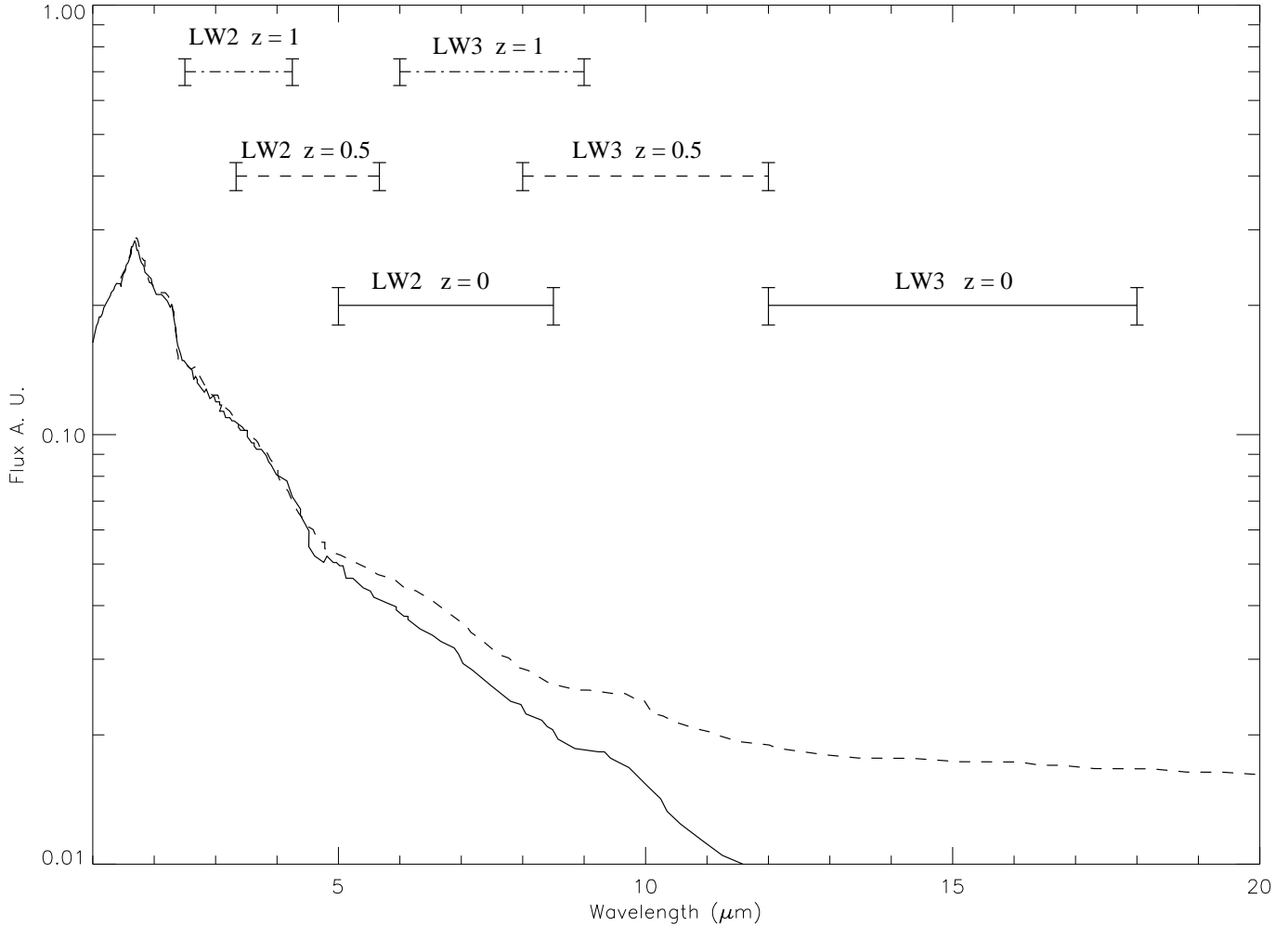


Fig. 2. Sketch of the mid IR emission of an old stellar population, compared with ISOCAM LW2 and LW3 filters bandpasses at various redshifts.

Solid line : model of the MIR emission of a 5 Gyr old stellar simple population, where dust envelopes of Mira and OH/IR stars are neglected (Bressan et al. 1998).

Dashed line : model of the MIR emission of a 5 Gyr old stellar simple population, for which the dust envelopes have been taken into account for the AGB phase, using silicate grains (Bressan et al. 1998).

The arbitrary units used for fluxes cannot be compared with those of Fig. 1, the relative importance of these emissions in various galaxies varies by factor of order 100.

3. Data acquisition

The HDF field is well suited for mid-infrared deep observations. It was selected for its low optical extinction, low HI column density and, most important fact for ISOCAM observations, low cirrus emission in the IRAS 100 μm maps (Williams et al. 1996). Moreover, it sits at high galactic latitude, and contains therefore only a few stars. Similar criteria were used to select fields for other ISOCAM deep surveys such as the IDSPCO program (Cesarsky & Elbaz 1996) or the DEEPPGPQ program (Taniguchi et al. 1997).

Table 1 describes the observation parameters for both filters. Each consist of three 8x8 rasters, which are partly overlapping. In both cases, the area covered is wider that

the HDF field, and even contains a large part of the flank-ing field for the LW3 observation, which was done with a larger pixel field of view (PFOV) and a greater raster step than the LW2 observation. If the detector had been ideal, *i. e.* with no memory effect and insensitive to cosmic rays, a very good sensitivity would be reached :

$$\sigma = \sqrt{\frac{\sum_{pixels} \sigma_{pixel}^2}{N_{exp}}}$$

where σ_{pixel} is the noise per readout for each ISOCAM pixel (it is therefore equal to the readout noise plus the photon noise, which is dominated in the case of faint sources by the background emission) , and N_{exp} is the number of exposures. One can easily compute the ideal

Table 1. ISO-HDF observation parameters. The main parameters for each raster and for the whole observation are listed

Parameter	LW2 (6.75 μm)	LW3 (15 μm)
Raster		
Integration time	10 s	5 s
Detector Gain	2	2
Number of exposures	9 or 10	19 or 20
Pixel field of view	3 "	6 "
Number of pointings	8x8	8x8
Step between two pointings	5"	9 "
Observation		
Number of rasters	3	3
Total area covered	10.45' ²	24.3' ²
Area of maximum sensitivity	0.98' ²	7' ²
Sensitivity (Jy/' ²)	$\sigma < 0.2$	$\sigma < 0.34$
Exposure time	> 1.94 hrs	> 2.25 hrs
Area of mean sensitivity	7.25' ²	21.5' ²
Sensitivity (Jy/' ²)	$\sigma < 0.5$	$\sigma < 1.37$
Exposure time	> 0.31 hrs	> 0.17 hrs

sensitivity of the ISO-HDF if one computes σ_{pixel} for each pixel : this is easily done by fitting a Gaussian distribution on the histogram of the each pixel, after having filtered it of all the low frequency components, because all the non ideal behaviour of ISOCAM occurs mostly at low frequency. At a 5σ level, one could reach 15 μJy in the LW3 band and 5 μJy in the LW2 band. The observation was designed to be as deep as possible, and with a good spatial resolution in order to be able to identify with confidence the optical counterparts of ISOCAM sources. The observations were therefore made using the microscan mode, that is by moving the camera by fraction of pixels between two raster steps. With a step of 5 arcsec and a PFOV of 3 arcsec, the final resolution of the ISOCAM map should reach 1 arcsec in LW2, and 3 arcsec in LW3.

Unfortunately, the long wavelength detector (LW) of ISOCAM is very sensitive to cosmic rays due to its thickness, and shows a transient behaviour. These two main drawbacks alter its efficiency in detecting faint sources. This is the reason why the PRETI method was developed.

4. Data reduction with the PRETI method

The two main difficulties for the detection of faint sources with the ISOCAM LW channel are mostly the cosmic ray effects and the transient behaviour (Starck et al. 1998). The PRETI method has been designed to overcome these two problems. The main idea of this method is to clean the cube of ISOCAM data as well as possible, before reconstructing the images and performing the source detection.

For the ISO-HDF data, as for all other data, the process goes through the following steps :

1. translate the raw data (CIER and IIPH files) in a raster structure containing the images, the ISOCAM configuration and the pointing information, using Cam Interactive Analysis (CIA).
2. convert the images in normalized units of ADU/G/s and subtract the dark current, with CIA.
3. correct the data for short time cosmic rays and mask the affected readouts.
4. clean the data for long term effect of cosmic rays.
5. subtract the baseline of each pixel.
6. compute the reduced images per raster pointings.
7. derive a flat-field from the baseline and correct the reduced images accordingly.
8. project each raster pointing on the sky.
9. perform a spatial detection on the final image.

The general method is described in Starck et al. (1998) and does not need to be detailed here. However, we discuss here some of the points above, either because they are very important, or because they need to be specifically adapted to each observation.

4.1. Long term effect of cosmic rays.

As explained in Starck et al. (1998), the impact of cosmic rays, apart from the high frequency response they induce in the LW detector, are sometimes followed by a slow decrease of the signal ('faders') or by a depletion in the detector gain ('dippers'). This behaviour is attributed to proton or α particle impacts on the detector, while simple 'glitches' are due to effects of the cosmic ray electrons. One has to be very careful in cleaning them, because they will produce false detection on the final map if they are not well removed.

This is especially true for the ISO-HDF observations, because only a small number of readouts are done per sky position, and because of the microscan observation mode. In this observation, one third of the 'faders' and 'dippers' lasts more than 60 readouts. This means that they last for more than 6 pointings (LW2) or 3 pointings (LW3). But each cosmic ray hits on average 4.5 adjacent pixels, that will more or less have the same behaviour. In a microscan, each position on the sky is observed by two adjacent pixels during two successive pointings. Figure 3 illustrates such an event : if the 'fader' effect is not corrected or masked out, it produces a spurious source when averaging all the readouts of a same pointing, because the flux appears to be above the 5σ noise level obtained on individual pointings. This example is taken from the LW3 observation : the two first pointings affected by the cosmic rays are less distant than the PSF FWHM. Since adjacent pixels of the one in the figure present the same behaviour, a spurious source will be 'detected', because faders will be co-added together.

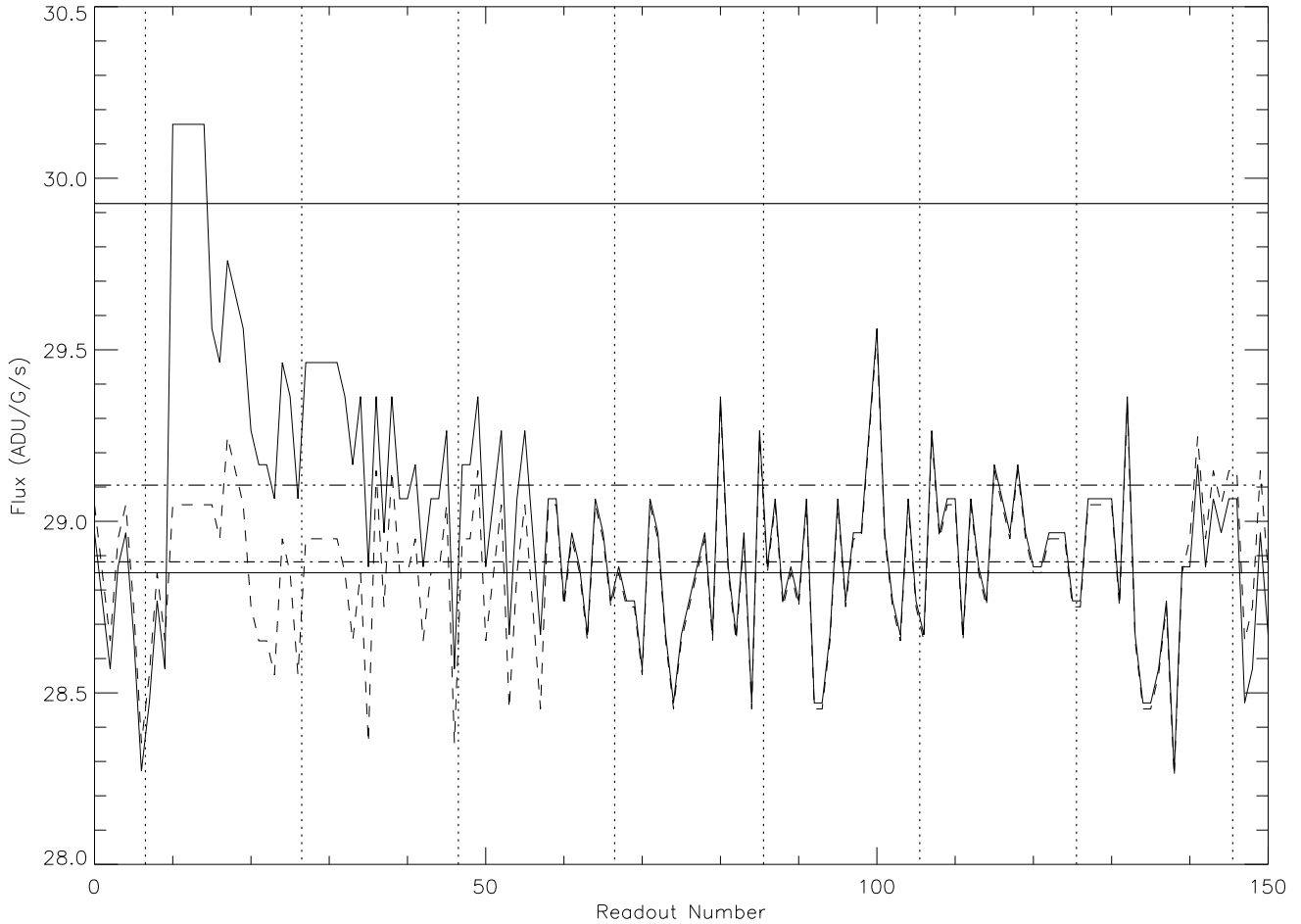


Fig. 3. Effect of a cosmic ray impact on the ISOCAM LW detector. The ‘glitch’ occurred on readout 9, and produced a ‘fader’ effect. The solid horizontal line at 28.85 ADU is the average background level. The solid horizontal line at 29.92 is the 5σ level of the noise. The dash-3 dots horizontal line is the average 5σ noise level after averaging all the readouts of a pointing. The dashed-dotted horizontal line is the 5σ level on the final raster map. The limits of each ISOCAM pointings are represented by dotted vertical lines. This ‘fader’ last for 3 pointings.

solid line : pixel response versus readout number, after correction for the short term effect of cosmic rays. Frames 9 to 15 and 26 to 30 have been masked out.

dashed line : final pixel response after correction for the long term effect of cosmic rays.

This effect is even more important in very deep observations where many raster positions are coadded together : ‘faders’ and ‘dippers’ are detected in the time history of the pixel, thus against a rather high noise level (see Fig. 3). On the contrary, sources will be detected on the co-added map, with a very low noise level that has been represented on the same figure. It may happen that the tail of cosmic ray effects, that were undetected in the temporal history, are coadded to themselves and therefore become visible on the final image as spurious structure.

In order to confront these problems for the HDF survey, we put very strong constraints on the deglitching process, that is :

1. The detection of structures in the temporal history of the pixel is done against 4σ of readout and photon noise, a lower level than for the usual PRETI method.
2. Each positive structure whose maximum is expressed at the same scale as a raster pointing is treated as a cosmic ray if :
 - a) a cosmic ray has been detected at its beginning (*i.e.* the two first readouts have been masked by the short deglitching process).
 - b) more than 50% of the readouts are already masked by the short deglitching process

This intends to avoid as much as possible false detections. There is the possibility that we might clean out a source, but this can be checked by the following method :

for each data set that we treat, we produce also raster maps where all the long term effects of cosmic rays are masked out instead of being corrected. Of course, this leads to far less sensitive maps since 20 to 40 % of the readouts are then eliminated. But this allows to check that the photometry of the remaining sources is consistent between the two reductions : this ensures that no real source was ‘cleaned out’ during the reduction. Indeed, in the end, we never find discrepancies in the flux of a given source by factors greater than 15%.

4.2. Baseline subtraction.

In order to correct for the long transient behaviour that takes place at the beginning of each observation (due to the change of the ISOCAM configuration), and to clean the data of the possible drifts of the detector, the PRETI method suppresses the baseline of each pixel’s time history. This is computed at larger temporal scales of the signal, at least larger than the scale of one raster pointing (Starck et al. 1998).

Because of the microscan observation, one has to extract the baseline at least two scales further for the ISO-HDF observation. Since the step between two raster pointings is about the same size as the FWHM of the ISOCAM PSF (9 arcsec at 15 μm and 4.5 at 6.75 μm), each source is seen by the same pixel during more than a raster pointing. In order to avoid to take some flux from the source into the baseline, it is computed two scales further as usual.

It is worth noting that the subtraction of the baseline frees the result of the reduction from the possible errors in the dark subtraction. Final images that are produced by the PRETI method are always on a zero background. Thus, such a method is only usable for observation on constant background, with no structure. This is the case for the zodiacal light emission, on an area as small as the HDF.

Nevertheless, it is possible to construct a background map of the observation. This map can be used to check the photometry by comparing the observed background with predicted values of models of zodiacal light.

4.3. Projection onto the sky.

Once each raster position has been averaged and flat-fielded, it is projected onto a sky map (RA, DEC, epoch 2000), whose resolution is computed according to the step size between raster pointings. The algorithm being used is derived from the classic ‘shift-and-add’ method. The intersection area of each CAM pixel with the sky map is computed, and added to it with a weight that is equal to this area times the square root of the number of pixels that were coadded to give the raster pointing image. That

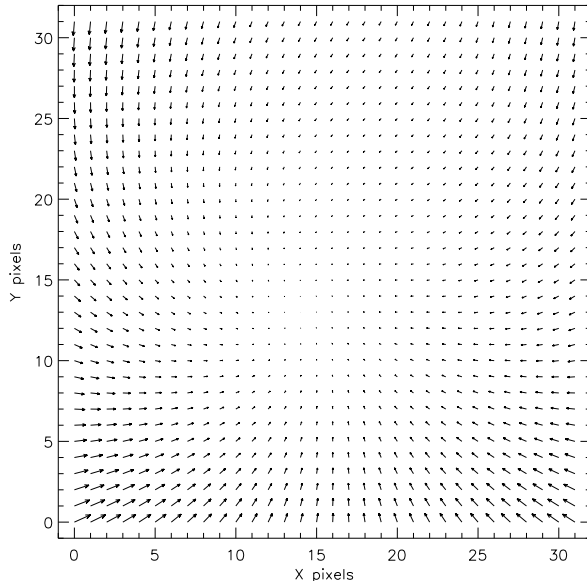


Fig. 4. ISOCAM distortion pattern for the LW10 6'' PFOV configuration. Each vector ends where the center of a pixel should fall if they were no distortion and starts from its observed position. The length of the vectors are at the scale of the plot : the effect is sometimes greater than the size of one pixel.

is :

$$R_{x,y} = \frac{\sum_{pointings} S_{(x,y,i,j)} \sqrt{N_{i,j}} I_{i,j}}{\sum_{pointings} S_{(x,y,i,j)} \sqrt{N_{i,j}}}$$

Assuming Gaussian distributions for pixels, one has for the noise map :

$$\sigma_{x,y} = \sqrt{\frac{\sum_{pointings} S_{(x,y,i,j)}^2 N_{i,j} \sigma_{i,j}^2}{\sum_{pointings} S_{(x,y,i,j)}^2 N_{i,j}}}$$

where $R_{x,y}$ is the value of the final raster map at (x,y), $S_{(x,y,i,j)}$ is the intercepted surface between ISOCAM pixel (i,j) and raster map pixel (x,y) and $N_{i,j}$ is the number of readouts that were averaged together to produce $I_{i,j}$, the image of the raster pointing. We choose to use $\sqrt{N_{i,j}}$ as weight rather than the R.M.S. computed during the coaddition because this is very poorly estimated (less than 10 readouts for the LW2 observation for example). Since the ideal detector should follow a Gaussian behaviour, its noise should vary as $\sqrt{N_{i,j}}$, which is a more reliable estimator. It is straightforward from the computation of $\sigma_{x,y}$ that the noise map against which we do our detection is highly inhomogeneous.

The projection of each raster pointing takes into account the field distortion of ISOCAM. It has been measured by our team (Aussel 1999), using the ISOCAM PSF

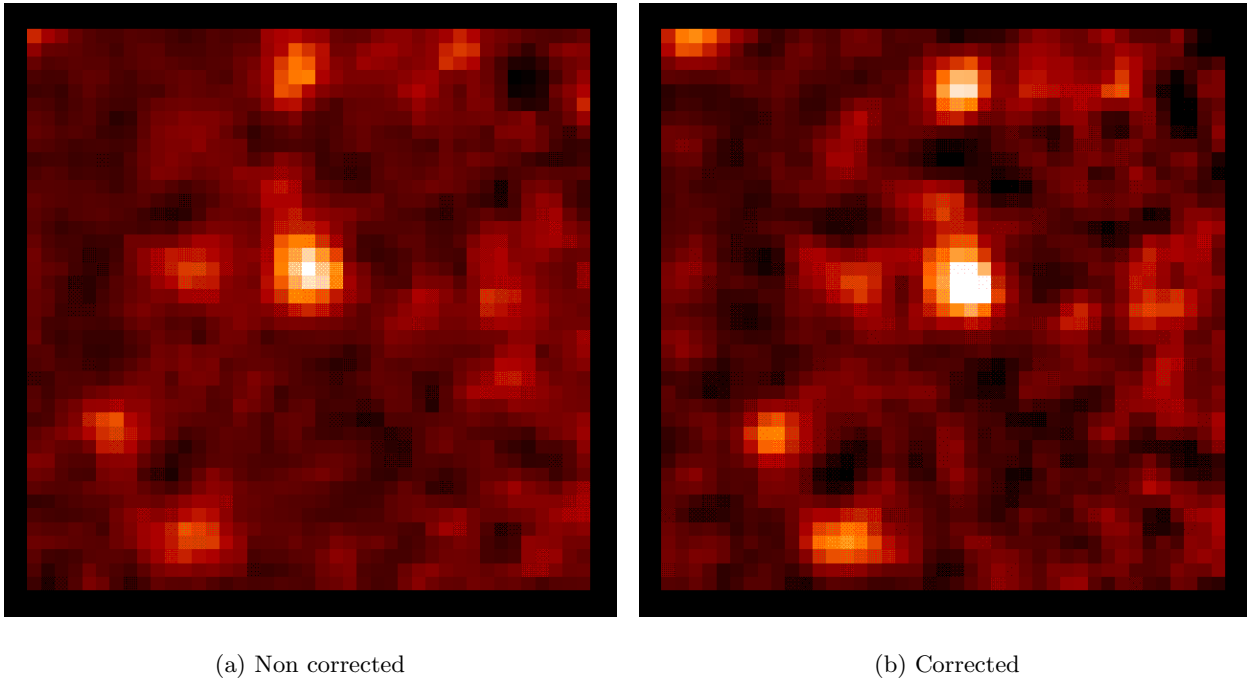


Fig. 5. Zoom on a part of the ISOCAM Hubble Deep Field observation at $15\mu m$. The same processing was applied to the two images, except for the correction of the distortion. Cuts on images are at the same level. Pixel size is $2''$.

model from Okumura (1997). Following the work done on the HST WFPC by Holtzman et al. (1995), we fit on our measurement a general polynomial of degree 3, that allows to compute for any pixel on the detector its position on the sky :

$$x_c = a_0 + a_1x + a_2y + a_3x^2 + a_4xy + a_5y^2 + a_6x^3 + a_7x^2y + a_8xy^2 + a_9y^3$$

$$y_c = b_0 + b_1x + b_2y + b_3x^2 + b_4xy + b_5y^2 + b_6x^3 + b_7x^2y + b_8xy^2 + b_9y^3$$

Figure 4 shows a map of the distortion of the LW channel of ISOCAM with the $6''$ PFOV and the LW3 filter, where each vector ends where the center of a pixel should fall if they were no distortion, and starts from its actual position. The length of the vectors are at the scale of the plot : at the lower corners of the array (lines 0 to 5), the effect is bigger than one pixel. If this effect were not taken into account, the sources would be smeared when coadding, and the final astrometry would be poor, reaching up to a $6''$ error. This is illustrated by Figure 5, where a zoom on the outskirts of one ISO-HDF raster is displayed without and with correction of distortion. On the borders and corners of the raster, the gain of signal over noise ratio is about 50 %.

The measurements at various wavelengths have shown that the distortion is a chromatic effect. We were able

to measure it for both filters and lenses of the ISO-HDF observation.

The flat fields are computed in CIA by making the assumption that the illumination of the detector is homogenous. Because of the field distortion, this is not truly the case since the pixel size is not uniform on the sky (the pixels at the edges of the array cover a wider surface). A new flat-field correction has to be applied in order to account for it. This flat-field is of the form :

$$F_{i,j} = \frac{S_{16,16}}{S_{i,j}}$$

where $S_{i,j}$ is the surface on the sky of pixel i,j . The pixel (16,16), which is the center pixel of ISOCAM LW array and therefore the least distorted, has been taken as reference. The images should therefore be divided by F before reprojecting on the sky.

4.4. Astrometric corrections

As the observations of the ISO-HDF have been performed in three separate rasters, one has to coadd all of the images in order to reach the maximum sensitivity. But this can only be done if the pointing of each raster is well known. This is not straightforward because of :

1. The absolute pointing accuracy (*i.e.* the 1σ error that can be made when acquiring a new target) of ISO is of 3 arcsec. This is much greater than the relative point-

ing accuracy, (*i.e.* the accuracy of pointings between two raster steps), which is less than 0.1 arcsec.

2. The lens wheel jitter. In order to avoid any mechanical blocking, the gear wheel has been designed with a small play. The position on which the lens stops is not fixed. It has been shown by the Cam Instrument Dedicated Team (CIDT) and by us that there are only two positions that each lens can take for a commanded position, probably at either side of the play. This can be very easily detected by a close inspection of the flat field derived from the data. If the leftmost column of the detector receives very little light, we know we are in the ‘left’ position. This jitter results in an offset of about 1.2 pixels from the optical axis, thus $\approx 7''$ with the $6''$ PFOV. It modifies also the distortion pattern of ISOCAM that has been measured for both positions. The only way to avoid such problem when coadding various rasters is to use the screw 129 and have them observed in a sequence in order to prevent any movement of the lens wheel between the two rasters. This was not the case for the ISO-HDF observations.

If all the observations suffer from the absolute pointing error, only one raster of the LW3 observation suffers from the second problem. The only way to coadd efficiently the rasters is to identify common sources in each of them and to compute an offset. These sources have to be bright enough to have a well definite position. In order to correct the absolute pointing error, good astrometric references are needed. The astrometry of the HST observation of the HDF has been established very carefully (Williams et al. 1996), but is not useful in our case : since the FWHM of ISOCAM PSF is large, there are in general several optical counterparts which could be associated to a single ISO-HDF source.

In order to solve this problem, we used the well known MIR/radio correlation (Helou et al. 1985). Since the HDF and the flanking fields have been observed at 8.4 GHz (Fomalont et al. 1997), we used this source list to match our brightest objects. We were successful in identifying at least 4 radio sources in each LW3 raster and at least one in each LW 2 raster. These sources are given in Table 2 together with the derived offsets.

4.5. Detection, source photometry and transients

As explained in Starck et al. (1998), the source detection is made on the final reprojected map, against the noise map, using a wavelet technique. We use a b-spline wavelet transform, and detect at each scale all pixels above a given threshold (τ_w) of the transformed noise map. In the ISO-HDF case, the final size of the pixels is $3''$ in LW3 ($1.5''$ in LW2) for a PSF that is $9''$ FWHM (resp. $4.5''$). We therefore ask the algorithm to perform the detection down to the 3^{rd} scale, that is over a box of 16 pixels, matching the PSF size. Since the maps are not square, some sources are

Table 2. ISO-HDF astrometric correction. The radio sources (Fomalont et al. 1997) used are listed for each field.

Raster	8.4 GHz	α offset	δ offset
LW2 Raster 2	3646+1404 3649+1313	$4.5'' \pm 2.0$	$+3.0'' \pm 2.0$
LW2 Raster 3	3649+1313	$0.0'' \pm 2.0$	$0.0'' \pm 2.0$
LW2 Raster 4	3644+1133	$+4.5'' \pm 2.0$	$+2.5'' \pm 2.0$
LW3 Raster 2	3634+1212 3634+1240 3644+1249 3646+1404 3646+1448 3649+1313	$0.0'' \pm 0.5$	$+4.0'' \pm 0.5$
LW3 Raster 3	3644+1249 3646+1404 3639+1313 3653+1139	$-0.7'' \pm 0.5$	$+4.0'' \pm 0.5$
LW3 Raster 4	3634+1212 3634+1240 3644+1249 3646+1404 3646+1448 3649+1313 3653+1139	$0.0'' \pm 0.5$	$-4.2'' \pm 0.5$

detected at the edges of the field due to non continuous limit conditions. Such sources are eliminated.

It is very important to note that the τ_w that is employed here describes the noise level of the detection map, but that this noise is not Gaussian. Since many treatments applied on the cube were done using median transform, and since the ‘dippers’ and ‘faders’ are highly non Gaussian, this means that one cannot relate a $3\tau_w$ detection to a 99.69 % confidence level, as it is the case for Gaussian statistics. Simulations only can give confidence levels for the value of the detection threshold.

The photometry of the objects can be measured in two ways. First, the detection program constructs an image of each object. The total flux in this image is computed. Second, a direct aperture photometry can be performed on the ISOCAM map. We have used the second method because simulations have shown us that for faint objects, the reconstruction using wavelets is not reliable. The measured Analog to Digital Units (ADU) are corrected to account for transients and for PSF. This correction has been obtained by simulations (see below). The corrected ADU are then translated to milli Jansky by using ISOCAM ‘cookbook’ conversion tables.

The response of the ISOCAM LW detector is affected by a transient when its illumination changes. The response reaches instantaneously a level corresponding to 60 % of the final, stabilized signal, the rise for the remaining 40 % being a slow exponential whose time constant depends

on the past history of the pixel. First order corrections have been produced, especially by Abergel et al. (1996). Transients are the source of two main problems :

1. an error in the photometry if the measured flux is not stabilized.
2. ‘ghost’ sources appear on maps after that the detector has observed a bright source ($\geq 500\mu Jy$).

Since the ISO-HDF has very small raster steps and no bright source is present in the field, the second point is not a problem in our case. Correcting transients has an effect on the time history of each pixel. Some glitches, with their slow decrease, mimic a transient behaviour, and could be treated inadequately by the correction algorithm. Since we detect these effects by criteria on their shape in the wavelet space, we might miss some of them after the correction of the transients. On the other hand, transient effects can be modeled, and taken into account when converting ADU to physical units. For these reasons, we do not perform any transient correction during the cleaning of the data cube.

Simulations were widely used to calibrate the translation of measured ADUs in ‘real’ ADUs, then in μJy and are detailed below.

5. Simulations

The PRETI method has been developed to detect faint sources in all ISOCAM data (if they are taken in fields where the background is more or less constant), but has to be tuned in order to work very efficiently, as shown in the previous section. This fine tuning has been done through various tests and simulations, that have proven to be very useful to ascertain detections, study the completeness, the number of false detections and to calibrate the source photometry.

In order to test the PRETI method, we have tried to build simulated data. These should be as near as possible of real ISOCAM data, that is, contain glitches, transients, and sources. A special attention has to be payed to the ‘fader’ and ‘dipper’ long term effects of glitches since they are the most limiting factor for the faint source detection. Unfortunately, no available model is able to reproduce accurately these behaviours of the LW detector. The only solution is to use real ISOCAM data to build simulations.

5.1. cosmic rays in simulated data

Cosmic ray effects are dependent of three parameters

1. the integration time because it is directly related to the mean number of cosmic rays that will hit the detector per readout.
2. the background emission, because in the long term effect a cosmic ray may affect the gain of the pixels (though this is not yet clearly established).

3. the period of the observation since the cosmic ray density varies along the orbit of the satellite as it crosses the radiation belts. We have noticed variations of 40 % in the number of ‘faders’ and ‘dippers’ between various observations, early part of the orbit being most affected.

For these reasons, data for the simulation are taken with the same integration time, same gain, same filter and zodiacal background as the observation that is to be simulated. Moreover, in order to avoid any modification of the time history of pixels, these data have to be taken on periods at least as long as the observation. For example, data taken on a shorter period and duplicated would cause discontinuities in the time history and produce spurious sources.

5.2. Suppression of real sources in the data set used for simulations.

Since we look for faint sources, it is very likely that the observations selected to be used for simulations will contain such sources.

The ideal case is when these are ‘staring’ observations, *i.e.* when the satellite points during a very long time at the same position. Since the flat-field is built directly from the observation, any source present in the field is cleaned during the operation.

One less ideal case is when the raster parameters of the observation are different from the simulated data. the sources in the simulation data set are blurred when the raster map is reconstructed with different steps. If there are bright sources in the simulated data, which would despite the blurring process still have a high S/N level, these can be masked out.

5.3. addition of sources

Point sources of various fluxes are added using the PSF model of M. Pérault and K. Okumura, that match well the measurements (Okumura et al. 1997). Each source flux is converted in ADU by using the ISOCAM cookbook. Object are randomly distributed on the raster map, at a precision of a tenth of a pixel, then each position on the detector array is recomputed, without taking the field distortion into account.

Each raster image is then translated into a data cube by using the transient model from Abergel et al. (1996), where the detector response D is a function of the incoming flux I with :

$$D(t) = rI(t) + (1 - r) \int_{-\infty}^t I(t') \exp\left(-\frac{t - t'}{\alpha/I(t')}\right) dt'$$

It is clear from this formula that the response depends on the intensity of the source and on the background, because the exponential time constant is a function of I . For this

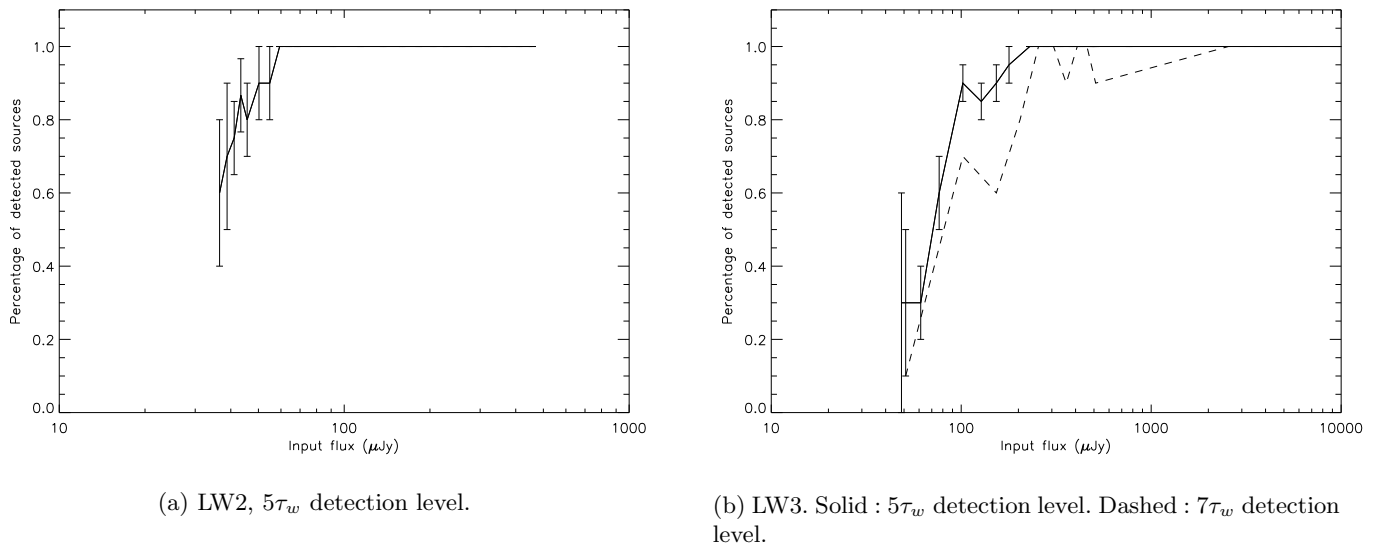


Fig. 6. Percentage of detected sources in simulations of the ISO-HDF, as a function of the input flux of the sources, for both filters

reason, we add to the simulated source images the median of the deglitched cube that is to be simulated before running the transient simulator. We subtract this image later, in order to have a simulated cube on a zero background, and add it to the raw data selected to perform the simulation.

5.4. ISO-HDF simulations

We have searched the ISOCAM calibration database for observations matching the ISO-HDF configurations. For the LW3 observation, we found a set of flat-field observations, called ‘FLAT16’ that were done with the same filter, the same lens and same integration time. Seven bright sources present in the field were masked out. Fainter sources have been blurred since this observation is a raster with half an array of raster step (16 pixels). We checked the PRETI method by running it completely on this set. We set our deglitching parameters in order to avoid any detection in that field (since their should be no source), except the ones that could be related to a source present in the original dataset. We also checked that the ‘fader’ and ‘dipper’ rate is about the same in both observations. This set of data is a perfect tool to build complete simulations. Since it is an empty field, we are able to study very carefully the level at which PRETI begins to give us false detections.

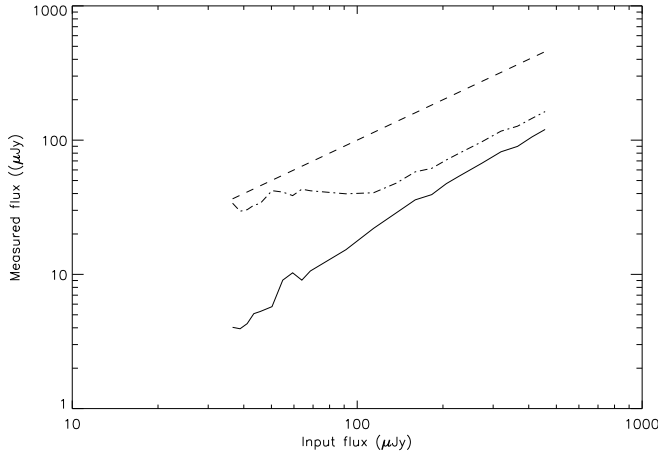
For the LW2 ISO-HDF, we could not find any satisfactory set of data : only a few calibration have been performed with an integration time of 10 s, and they are always short ones. We eliminated also data from our ID-SPCO survey program that were matching all the configuration requirements, because we found a rate of long

term effect cosmic rays about 20 % higher : this causes severe differences in the sensitivity that can be reached by an observation. Since our first reductions show us that the source density is not very high in the ISO-HDF LW2 observation, we decided to use these data themselves for the simulations. The drawback is that this prevents us to fully study the confidence level and the false detections.

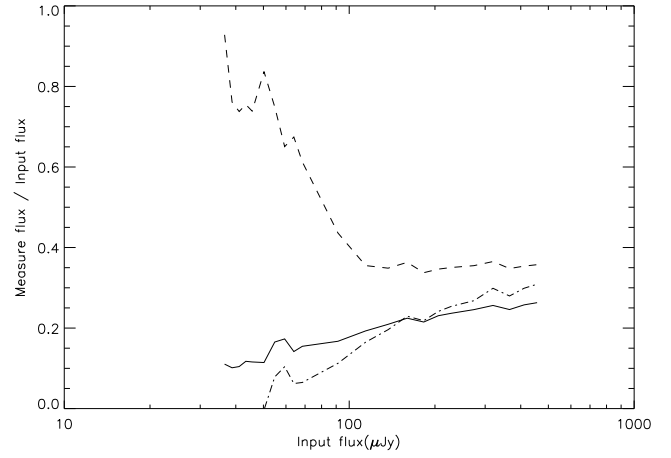
We performed two kinds of simulations. First, 10 sources of a given flux were randomly added, and the operation was repeated from 1 mJy to 100 μJy by steps of 100 μJy, and from 100 to 10 μJy by steps of 10 μJy. This allowed us to investigate our detection limits and to calibrate our source photometry. Finally, we performed simulations containing a wide range of fluxes, more or less matching number count models, in order to test the completeness of the method.

5.5. Simulation results on the ISO-HDF

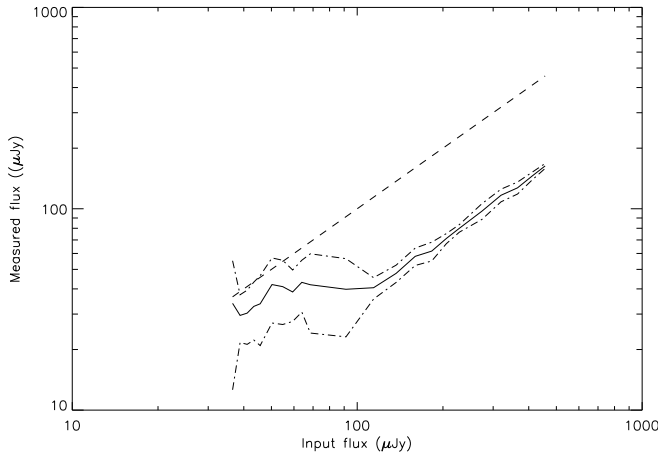
Figure 6 presents the results of our counts on simulated data for LW2 (a) and LW3 (b). For the LW2 filter, all added sources in the field are detected down to 60 μJy for a 5 τ_w detection, showing that we are complete at this level. However, this result does not take into account confusion. A faint source is not detected if it is too close to a bright one (~ 9” in LW3, depending on the relative brightness of the two sources). This effect has to be taken into account when deriving number counts. For the LW3 observation, the 99.9% completion is obtained above 200 μJy, for a 5τ_w detection and stays above 85% at 100 μJy. 7τ_w detection, that are more reliable in terms of avoiding false detections, are only 99.9% complete above 1 mJy, but stay of the order of 90 % down to 220 μJy. We could not



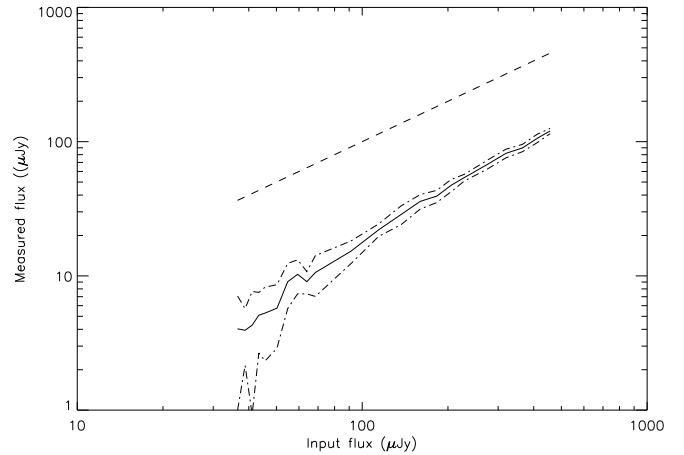
(a) Measured flux as a function of input flux for 2 photometry methods. Solid : 2 pixel aperture photometry (3''). Dot-dashed : wavelet photometry. Dashed : the identity curve.



(b) Ratio of measured flux over real flux as a function of the real flux. Solid : 2 pixel aperture photometry (3''). Dot-dashed : 3 pixel aperture photometry (4.5''). Dashed : wavelet photometry.



(c) Measured flux as a function of input flux for the wavelet method. Solid : measure. Dash-dotted : 1σ error on measure. Dotted : Identity.



(d) Measured flux as a function of input flux for 2 pixel (3'') aperture photometry. Solid : measure. Dash-dotted : 1σ error on measure. Dotted : Identity.

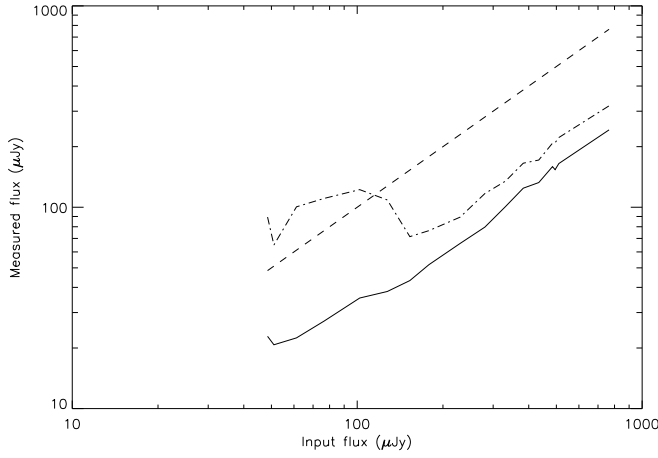
Fig. 7. Photometry results of LW2 simulations. Comparison of photometric methods and errors.

measure the number of false detections in the LW2 band since we used the data set itself to do the simulations. Since PRETI is run with the same arguments on both sets, we assume that the difference should be small between the two filters and tune our criteria according to LW3.

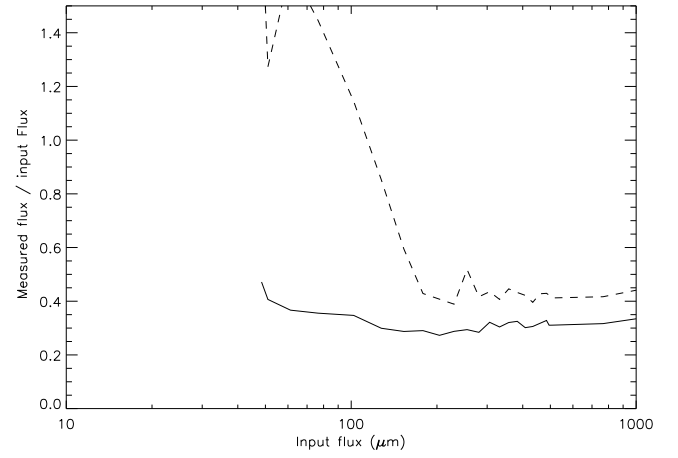
Figures 7 and 8 show the calibrations curves deduced from simulations, *i.e.* the relation between the measured flux to the real flux that was simulated, for two measurement methods : (1) an aperture photometry taking a radius of 3'' for LW2 and 6'' for LW3 (two pixels in each case), (2) the integrated flux of the objects recon-

structed by our wavelet based detection program (Starck et al. 1998). The two methods display very different behaviors for the faint end of the plots.

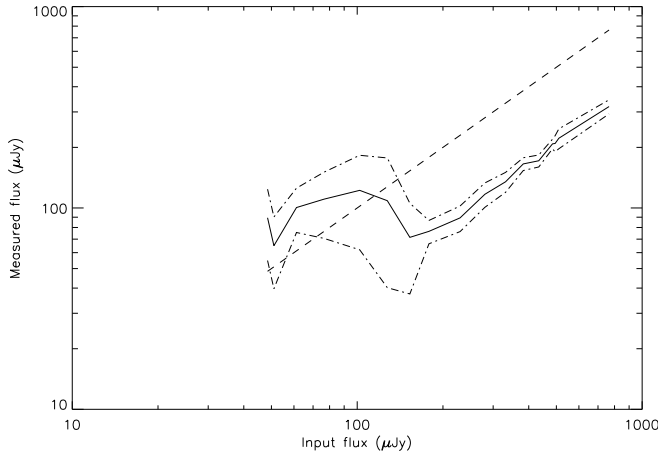
Photometry on wavelet reconstructed objects (panels (c)) shows a non-linearity effect for input fluxes below 100 μJy in LW2 (*resp.* 200 μJy in LW3). Above these levels, the ratio of the measured flux over the input flux is roughly constant (~ 0.45 for LW2). We interpret this factor in terms of the effect of transients (factor of 0.6) , and by the fact that only the central core of the PSF is reconstructed by the algorithm (factor of 0.8), thus giv-



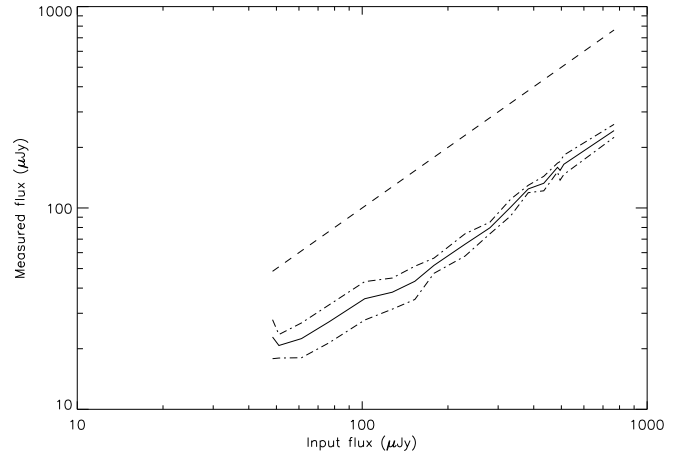
(a) Measured flux as a function of input flux for 2 photometry methods. Solid : 2 pixels aperture photometry (3''). Dot-dashed : wavelet photometry. Dashed : the identity curve.



(b) Ratio of measured flux over real flux as a function of the real flux. Solid : 2 pixel aperture photometry (3''). Dot-dashed : wavelet photometry.



(c) Measured flux as a function of input flux for the wavelet method. Solid : measure. Dash-dotted : 1σ error on measure. Dotted : Identity.



(d) Measured flux as a function of input flux for 2 pixels (3'') aperture photometry. Solid : measure. Dash-dotted : 1σ error on measure. Dotted : Identity.

Fig. 8. Photometry results of LW3 simulations. Comparison of photometric methods and errors.

ing a theoretical correction of 0.48. Below these levels, the non-linearity is explained by the fact that the wavelet analysis program reconstructs objects with extended low levels wings. This effect might be due to the fact that we use a b-spline wavelet transform of our map that does not match closely enough the ISOCAM PSF. We note that the non-linearity is more marked for LW3 than for LW2 where the PSF is less extended, and is therefore closer to the wavelet shape. For the last filter, the measured level stays constant at $30 \mu\text{Jy}$ while it rises in the first one for decreasing fluxes. The reason for this difference is not clear,

but might be explained by the confusion of the observations in the LW3 map, or by residual glitches¹. This non-linearity prevents to use the “wavelet” photometry for low levels objects, thus this method is not appropriate for the HDF data set.

Aperture photometry (panels (d)) does not display such non-linearity. In LW2, the ratio of the measured flux over the input flux decreases as the input flux decreases. The explanation for this behaviour is the follow-

¹ the only way to test this hypothesis is to achieve clean simulations of empty fields !

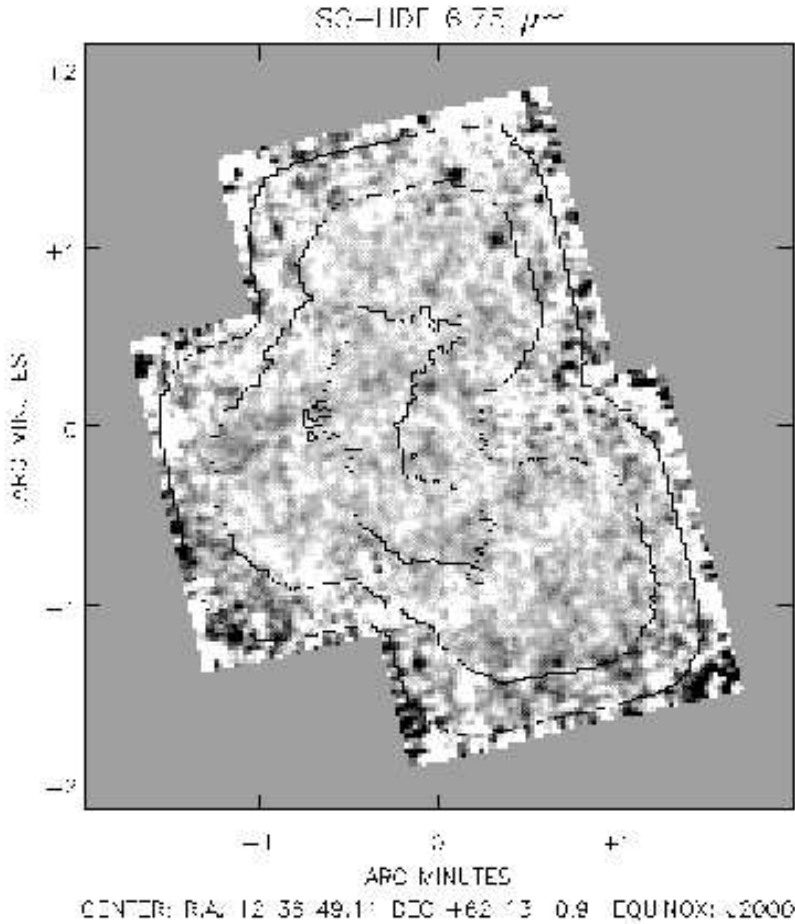


Fig. 9. Map of the ISO-HDF LW2 filter ($6.75 \mu\text{m}$). Resolution is of $1.5''/\text{pixel}$. Contours are $5 \tau_w$ detection levels at 35, 50 and $100 \mu\text{Jy}$

ing : when the flux decreases, the outer pixels of the central core of the PSF are more and more dominated by the noise, and the summed flux contains therefore negative terms. Indeed, due to the baseline subtraction, a few readouts are slightly negative before and after the source, (the background level is overestimated). Therefore, the average level on the final map around the source is slightly negative. This effect is illustrated in figure 7 (b) where a 3 pixel radius aperture photometry has also been drawn (dash-dotted curve). For this method, the ratio at high flux is larger than for a 2 pixel radius aperture (more of the central core is taken into account), but decreases more abruptly toward faint fluxes, because more noise and negative values are integrated in the aperture. We note that at high flux, the ratio between the measured flux in the 3 pixels and 2 pixels apertures is $\sim 0.3/0.25 = 1.2$, in good agreement with the PSF model that predicts 1.209. Again for this photometric method, the behaviour of the LW3 filter is slightly different, because the slope of the calibration curve is less steep toward faint fluxes. The change of slope

occurs at the same level ($200 \mu\text{Jy}$) where the “wavelet” method begin to be non-linear. This indicates that the same process is at work for both methods, but that aperture photometry is less affected. For these reasons, we have used a two pixel aperture photometry for the HDF.

6. Results on the ISO-HDF

Figures 9 and 10 present the reduced map of the ISO-HDF LW2 and LW3. Many sources are clearly visible on the latter, while the former appears almost empty. Various sensitivity levels have been overlayed on the maps, showing that the noise is very inhomogeneous. These sensitivity levels were computed by comparing the noise level at each scale with the wavelet coefficients of a point source image, the source being centered on a pixel. Thus, these levels give only an indication. If a source fell between two pixels, its wavelet coefficients at lower scales (high spatial frequencies) is lower, while those at higher scales (low spatial frequencies) are higher. Since the noise decreases when

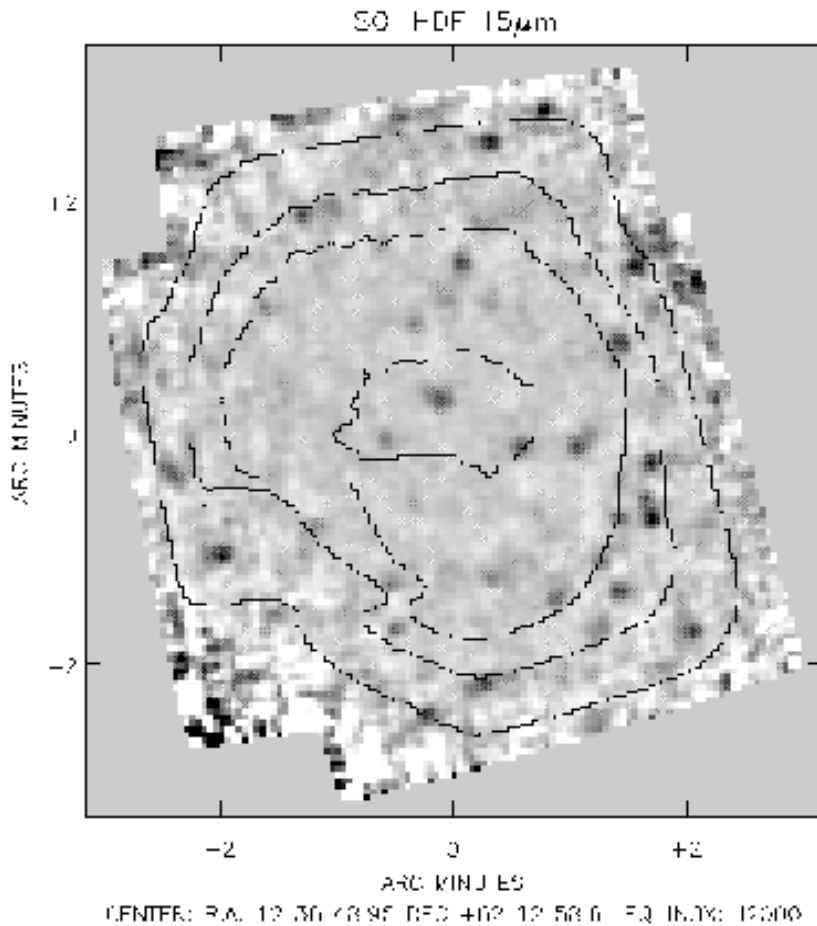


Fig. 10. Map of the ISO-HDF LW3 filter ($15 \mu\text{m}$). Resolution is of $3''/\text{pixel}$. Contours are $5 \tau_w$ detections levels at $35, 50, 100$ and $200 \mu\text{Jy}$

considering higher scales (Starck et al. 1998), sources can in fact be detected at fluxes lower than the levels shown on figures 9 and 10.

6.1. Source catalog

Table 3 gives the catalog of detected sources at $6.7 \mu\text{m}$ (LW2 filter) and $15 \mu\text{m}$ (LW3) above a secure $7\tau_w$ of photon and readout noise. The first column is our ISO-HDF identifier, the second and third column are the right ascension and declination of the object. The pointing accuracy is of 1 pixel on the final map, *i.e.* $3''$ for the LW3 image and $1.5''$ for the LW2 image. Columns 4 and 5 give the objects fluxes in the LW2 band in μJy and $\text{ADU}/\text{G}/\text{s}$, that is in analog to digital unit per second divided by the instrument gain, and columns 7 and 8 give the same in the LW3 band. Columns 6 and 9 give the detection level in the LW2 (*resp.* LW3) band. Column 10 identifies the field where the object is observed (HDF or flanking field). Column 11 gives the spectrometric redshift when avail-

able. Finally, column 12 give the morphological type of the object.

The redshift and morphological type of each ISOCAM source depend on the identification of its optical counterpart. Hopefully, our astrometric correction is good enough to allow us a good superposition with optical images, at a scale of 1 pixel. This is clearly visible on figures 11 and 12 where we have overlayed our ISOCAM maps on the KPNO IRIM deep K exposure² (Dickinson et al. in prep), as well as on figure 13 where we have overlayed the LW3 ISOCAM map and the LW2 detections on the color composite image of the HDF observed by HST from Williams *et al.* (1996). In most cases, the ISOCAM source matches an IR or optical source, and the identification is easy. However, due

² Based on observations made at the Kitt Peak National Observatory, National Optical Astronomy Observatories, which is operated by the Association of Universities for Research in Astronomy, Inc. (AURA) under cooperative agreement with the National Science Foundation.

Table 3. PRETI main source list for the ISOHDF observations at 6.5 μ m (LW2) and 15 μ m (LW3). All sources are detected at $7\tau_w$ above readout and photon noise. (1) : Source identification ‘PM3’ is for PRETI Main list LW3, ‘PM2’ for PRETI Main list LW2 . (2),(3) : source position for the J2000.0 equinox. (4) : source flux in microJansky in the LW2 filter with error bar or upper limit ($5\tau_w$). A ‘-’ indicates that the source is not in the LW2 field. (5) : source flux in ADU/G/s in a 3” aperture. (6) : detection level ($n\tau_w$) in the LW2 image.(7) : source flux in microJansky in the LW3 filter with error bar or upper limit ($5\tau_w$). (8) : source flux in ADU/G/s in a 6” aperture. (9) : detection level ($n\tau_w$) in the LW3 image. (10) : Identifier of the HST field in which the source falls (hd stands for HDF, others for flanking fields). (11) : spectroscopic redshift with source indicated by a note. (c) : data from Cohen et al. (1996), (p) : data from Phillips et al.(1997), (i) : compiled in Cowie et al. (1997), (h) data from Hogg et al. (1977b). (12) : morphological type of the object. ‘(i)’ indicates a type compiled in Cowie et al. (1997), ‘(p)’ type from Phillips et al. (1997), otherwise determined by us. E : Elliptical or S0 galaxy. S : spiral. M : merger. P : peculiar/irregular, C : compact object from Phillips et al. (1997) sample, A : active nuclei galaxy, G : source falls on a group. U : unknown type. N : no optical counterpart. A ‘?’ indicate a dubious type identification.

Id ⁽¹⁾	α ⁽²⁾ (J2000)	δ ⁽³⁾ (J2000)	LW2 ⁽⁴⁾ μ Jy	LW2 ⁽⁵⁾ ADU/G/s	$N\tau_w$ (6)	LW3 ⁽⁷⁾ μ Jy	LW3 ⁽⁸⁾ ADU/G/s	$N\tau_w$ (9)	F (10)	z ⁽¹¹⁾	T ⁽¹²⁾
HDF_PM3.1	12 36 31.4	+62 11 15	-	-	-	355 ⁺⁴⁰ ₋₆₀	0.211	7	sw	-	P
HDF_PM3.2	12 36 34.4	+62 12 12	-	-	-	448 ⁺⁶⁸ ₋₅₉	0.284	7	sw	-	M
HDF_PM3.3	12 36 34.4	+62 12 42	-	-	-	363 ⁺⁷⁹ ₋₃₈	0.227	7	iw	1.219 (c)	P
HDF_PM3.4	12 36 34.8	+62 12 24	-	-	-	267 ⁺⁵⁹ ₋₆₂	0.155	7	sw	0.562 (c)	S
HDF_PM3.5	12 36 35.6	+62 14 24	-	-	-	441 ⁺⁴³ ₋₈₂	0.264	7	iw	-	S
HDF_PM3.6	12 36 36.5	+62 13 48	-	-	-	353 ⁺⁴⁰ ₋₆₆	0.210	7	iw	0.960 (p)	CA ^(p)
HDF_PM3.7	12 36 36.9	+62 11 36	< 135	-	-	300 ⁺⁶² ₋₆₇	0.115	7	sw	0.078 (c)	S
HDF_PM3.8	12 36 36.9	+62 12 15	< 113	-	-	202 ⁺⁵⁸ ₋₅₀	0.116	7	sw	-	S
HDF_PM3.9	12 36 38.2	+62 11 18	-	-	-	212 ⁺⁵⁸ ₋₅₅	0.120	7	sw	-	G
HDF_PM3.10	12 36 38.2	+62 11 51	< 61	-	-	212 ⁺⁵⁸ ₋₅₅	0.119	7	sw	-	U
HDF_PM3.11	12 36 39.9	+62 12 51	< 64	-	-	302 ⁺⁶⁷ ₋₅₅	0.180	7	iw	-	E
HDF_PM2.1	12 36 40.4	+62 11 41	127 ⁺⁹⁹ ₋₆₁	0.021	7	< 72	-	-	hd	0.585 (i)	E
HDF_PM3.12	12 36 41.2	+62 11 33	< 66	-	-	236 ⁺⁶¹ ₋₅₈	0.133	7	hd	0.089 (c)	P
HDF_PM3.13	12 36 41.2	+62 14 21	-	-	-	76 ⁺⁷¹ ₋₁₉	0.052	7	iw	-	P
HDF_PM3.14	12 36 41.6	+62 12 06	< 37	-	-	52 ⁺³⁴ ₋₀₉	0.042	7	hd	0.432 (c)	S ⁽ⁱ⁾
HDF_PM3.15	12 36 43.0	+62 12 18	< 37	-	-	49 ⁺³⁶ ₋₀₉	0.036	7	hd	0.454 (c)	S ⁽ⁱ⁾
HDF_PM2.2	12 36 43.4	+62 11 42	185 ⁺⁹⁹ ₋₂₅	0.028	7	< 66	-	-	hd	0.764 (c)	E ⁽ⁱ⁾
HDF_PM3.16	12 36 43.8	+62 14 00	< 68	-	-	50 ⁺³³ ₋₀₉	0.040	7	iw	0.201 (c)	S
HDF_PM3.17	12 36 44.2	+62 12 51	< 50	-	-	282 ⁺⁶⁰ ₋₆₄	0.163	7	hd	0.557 (c)	M ⁽ⁱ⁾
HDF_PM3.18	12 36 44.7	+62 14 51	< 329	-	-	105 ⁺⁹⁴ ₋₂₁	0.076	7	nw	-	N
HDF_PM3.19	12 36 46.4	+62 11 42	88 ⁺⁴⁵ ₋₈₀	0.009	5	170 ⁺⁵⁹ ₋₄₂	0.097	7	hd	1.016 (c)	S ⁽ⁱ⁾
HDF_PM3.20	12 36 46.4	+62 14 06	191 ⁺⁴¹ ₋₈₆	0.032	7	107 ⁺⁹⁵ ₋₂₀	0.078	7	hd	0.960 (c)	S ⁽ⁱ⁾
HDF_PM3.21	12 36 46.4	+62 15 30	-	-	-	418 ⁺⁹¹ ₋₉₄	0.250	7	nw	0.851 (p)	M
HDF_PM3.22	12 36 46.8	+62 10 48	-	-	-	327 ⁺³⁹ ₋₆₃	0.195	7	se	-	N
HDF_PM3.23	12 36 47.2	+62 14 48	< 179	-	-	144 ⁺⁷² ₋₄₇	0.084	7	nw	-	N
HDF_PM3.24	12 36 48.5	+62 14 27	254 ⁺⁷¹ ₋₇₃	0.051	7	307 ⁺⁶² ₋₆₇	0.177	7	nw	-	E
HDF_PM3.25	12 36 49.3	+62 11 48	< 53	-	-	75 ⁺⁷¹ ₋₁₉	0.052	7	hd	0.961 (h)	S
HDF_PM2.3	12 36 49.4	+62 13 47	41 ⁺⁶⁶ ₋₃₀	0.005	7	< 52	-	-	hd	0.089 (c)	E ⁽ⁱ⁾
HDF_PM3.26	12 36 49.4	+62 14 06	< 40	-	-	150 ⁺⁷⁴ ₋₄₈	0.087	7	hd	0.752 (c)	S ⁽ⁱ⁾
HDF_PM3.27	12 36 49.8	+62 13 15	136 ⁺⁶⁸ ₋₅₇	0.019	7	320 ⁺³⁹ ₋₆₂	0.191	7	hd	-	G
HDF_PM3.28	12 36 51.1	+62 10 30	-	-	-	341 ⁺⁴⁰ ₋₆₅	0.204	7	se	0.410 (i)	P
HDF_PM3.29	12 36 51.9	+62 12 21	< 36	-	-	48 ⁺³² ₋₀₉	0.038	7	hd	0.299 (c)	S ⁽ⁱ⁾
HDF_PM3.30	12 36 51.9	+62 13 54	< 39	-	-	151 ⁺⁷⁴ ₋₆₈	0.088	7	hd	0.557 (c)	M ⁽ⁱ⁾
HDF_PM3.31	12 36 53.2	+62 11 15	-	-	-	174 ⁺⁵⁹ ₋₄₃	0.099	7	se	-	P?G?
HDF_PM3.32	12 36 53.7	+62 11 39	-	-	-	180 ⁺⁶⁰ ₋₄₃	0.103	7	ie	-	G
HDF_PM3.33	12 36 54.1	+62 12 54	< 36	-	-	179 ⁺⁶⁰ ₋₄₃	0.102	7	hd	0.642 (c)	S ⁽ⁱ⁾
HDF_PM3.34	12 36 54.1	+62 13 57	< 42	-	-	47 ⁺³¹ ₋₀₉	0.038	7	hd	0.849 (i)	S ⁽ⁱ⁾
HDF_PM3.35	12 36 57.1	+62 11 27	-	-	-	75 ⁺⁷¹ ₋₁₉	0.052	7	ie	-	N
HDF_PM3.36	12 36 57.5	+62 13 00	< 38	-	-	60 ⁺⁴⁰ ₋₂₃	0.043	7	hd	0.474 (c)	M ⁽ⁱ⁾
HDF_PM3.37	12 36 58.0	+62 14 54	-	-	-	225 ⁺⁶⁰ ₋₅₆	0.127	7	ne	-	N
HDF_PM3.38	12 36 58.8	+62 14 24	< 187	-	-	52 ⁺³⁴ ₋₀₉	0.041	7	ne	-	N
HDF_PM3.39	12 36 59.2	+62 12 09	< 66	-	-	157 ⁺⁷⁵ ₋₄₉	0.091	7	ie	-	P
HDF_PM3.40	12 37 00.1	+62 14 51	-	-	-	295 ⁺⁶¹ ₋₆₆	0.170	7	ne	0.761 (c)	M

Continued on next page...

Continued from previous page...

Id ⁽¹⁾	α ⁽²⁾ (J2000)	δ ⁽³⁾ (J2000)	LW2 ⁽⁴⁾ μJy	LW2 ⁽⁵⁾ ADU/G/s	$N\tau_w$ (6)	LW3 ⁽⁷⁾ μJy	LW3 ⁽⁸⁾ ADU/G/s	$N\tau_w$ (9)	F (10)	z ⁽¹¹⁾	T ⁽¹²⁾
HDF_PM3_41	12 37 01.8	+62 13 24	< 97	-	-	83^{+76}_{-19}	0.058	7	ie	0.410 ^(c)	P
HDF_PM3_42	12 37 02.2	+62 11 24	-	-	-	162^{+76}_{-49}	0.095	7	ie	0.136 ^(p)	S
HDF_PM3_43	12 37 03.1	+62 12 18	< 296	-	-	49^{+74}_{-30}	0.045	7	ie	-	N
HDF_PM3_44	12 37 03.1	+62 14 03	-	-	-	144^{+73}_{-47}	0.084	7	ne	1.242 ^(c)	P
HDF_PM3_45	12 37 06.1	+62 11 54	-	-	-	431^{+43}_{-80}	0.258	7	ie	0.904 ^(p)	S
HDF_PM3_46	12 37 06.5	+62 13 33	-	-	-	86^{+78}_{-37}	0.060	7	ie	0.753 ^(c)	U

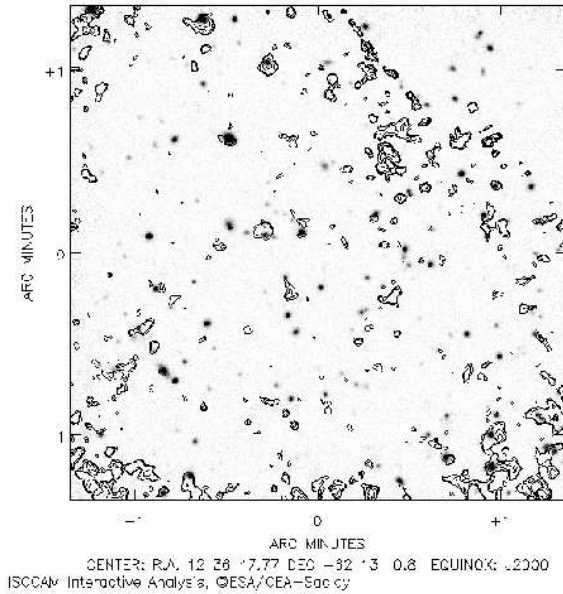


Fig. 11. Comparison near-IR/LW2 filter. The contours of the central part of the LW2 map have been overlaid on the IRIM K map. Contours levels begin at $1.0 \mu\text{Jy}$ with steps of $2 \mu\text{Jy}$.

to the large PSF ($15''$ at $15\mu\text{m}$) of ISOCAM, sometimes more than one object could be associated with our detection. Figure 14 displays an example of such a case : the main peak of source HDF_PM3_6 correspond to two objects. In this particular case, we have taken the brightest object in K as counterpart. When K data are not available, we have used the ‘G’ (for group) symbol in our table, because we could not determine the right counterpart.

Looking closely at figure 14, one can see that the object HDF_PM3_6, detected as a whole, displays substructures. Our detection program does not separate the various components of the source because it is not robust against blending : to avoid detection of cosmic ray residuals, we choose to perform the detection starting from the second scale of the wavelet transform of our map, *i.e.* on scales of the order of 3 pixels that prevent us to separate very closeby sources, especially if they are much weaker than the main detection. However, in some cases, this separation can be done by hand, when blending is weak enough to allow for the separation of the source (Rayleigh crite-

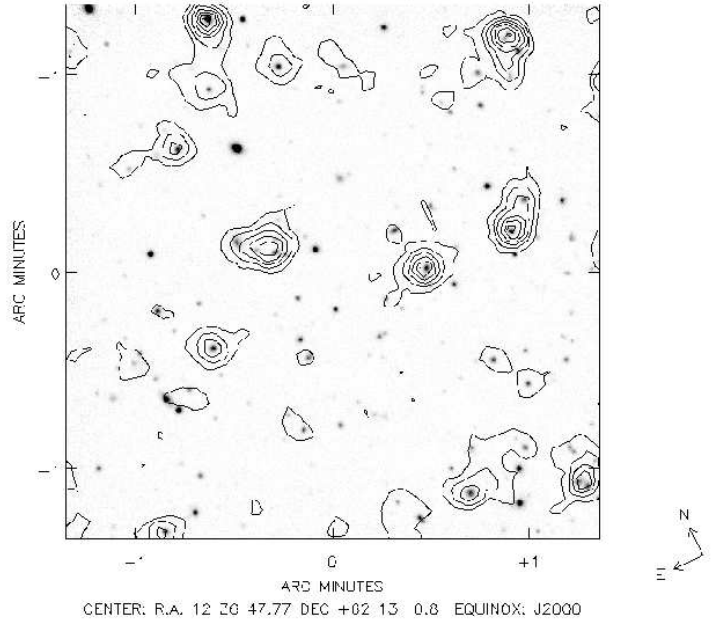


Fig. 12. Comparison near-IR/LW3 filter. The contours of the central part of the LW3 map have been overlaid on the IRIM K map. Contour levels begin at $1.5 \mu\text{Jy}$ with steps of $2 \mu\text{Jy}$.

ria). This is the case for source HDF_PM3_6, for which 4 extensions are visible on figure 14, South and East of the main peak. These extensions are in our supplementary list (see table 4) with the names HDF_PS3.6a, HDF_PS3.6b, *etc....* Figure 15 displays another case where the separation is possible, for source HDF_PM3_17 . Figure 16 displays a closeup on source HDF_PM3_27 : the source is extended, with multiple counterparts, but we failed to separate the various contributions. We note however that this source is the radio source 3639+1313 in the catalog of Fomalont at al. (1997), whose contours in the radio map (Richards et al. 1997) are also clearly extended.

We produced a supplementary list of sources with these extensions of reliable sources, together with results of PRETI at lower detection levels (6 and $5 \tau_w$), that is listed in table 4. However, this catalog may contain spurious detections, as it is certainly the case for sources HDF_PS3_13 and HDF_PS3_29, with fluxes below $10 \mu\text{Jy}$. In the future, we expect to obtain data of a long staring observation on an empty field. Using this observation as a basis for simu-

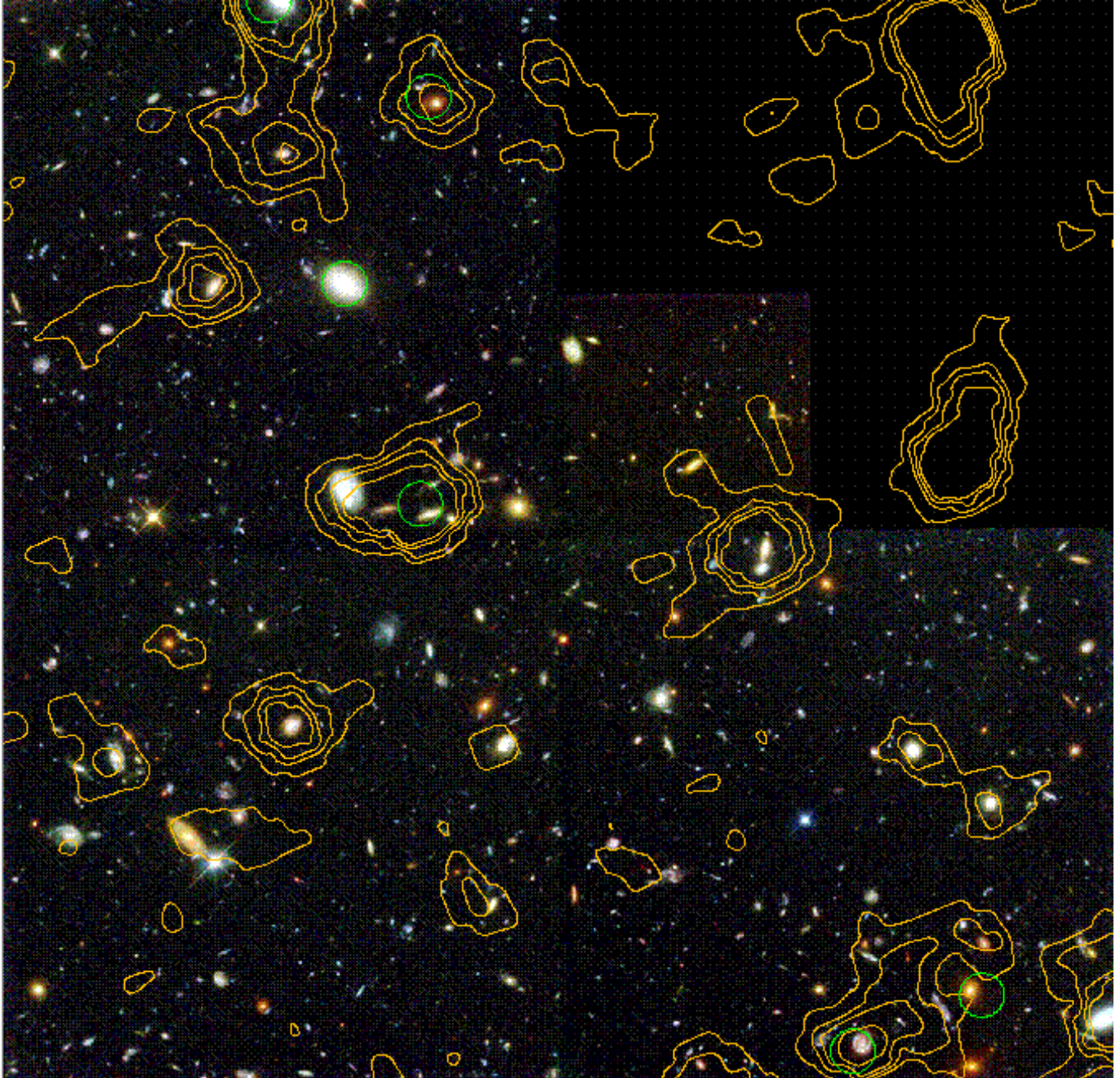


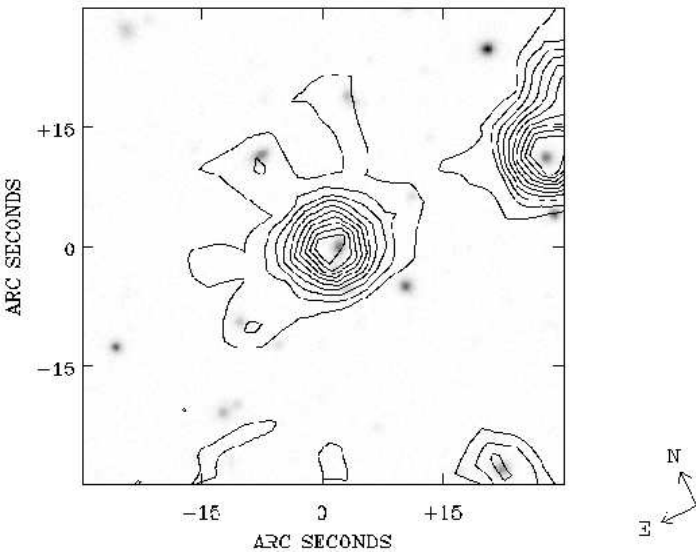
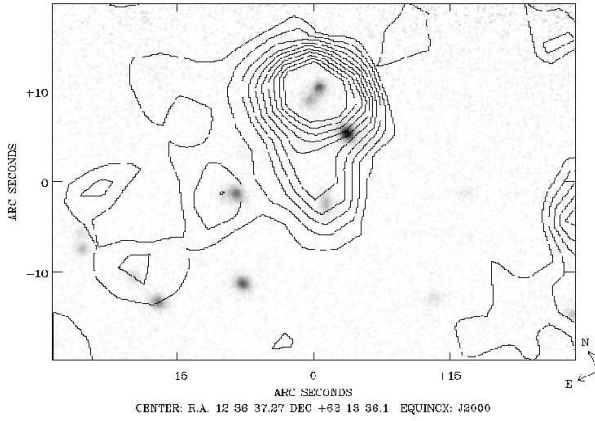
Fig. 13. Overlay of the ISO-HDF observation on the HDF color composite image produced by Williams *et al.* (1996) from the F450W, F606W and F814W images obtained with HST. Orange contours : contours of the 15 μm (LW3) ISOCAM observation. Contours levels begin at 1.0 μJy with steps of 2 μJy . Green circles : ISOCAM 6.75 μm (LW2) detections.

lations, we hope to be able to obtain higher reliability on the sources at these low level of flux.

6.2. Catalog properties.

Our main source list consist in 49 objects detected above a $7\tau_w$ detection threshold in both filters. 42 sources are detected at 15 μm only, 4 at 6.5 and 15 μm , and 3 at

6.5 μm only. Since the LW3 field is larger than the LW2 field, this last number means that 21 of the LW3 sources are not detected in LW2. The supplementary list adds 51 sources to this catalog for a total of 100 objects. 47 are observed in the LW3 filter only, and 4 in the LW2 filter only. None are detected in both filters, 15 of the LW3 sources that could be visible in the LW2 field remain undetected. For these missed detection, we have computed

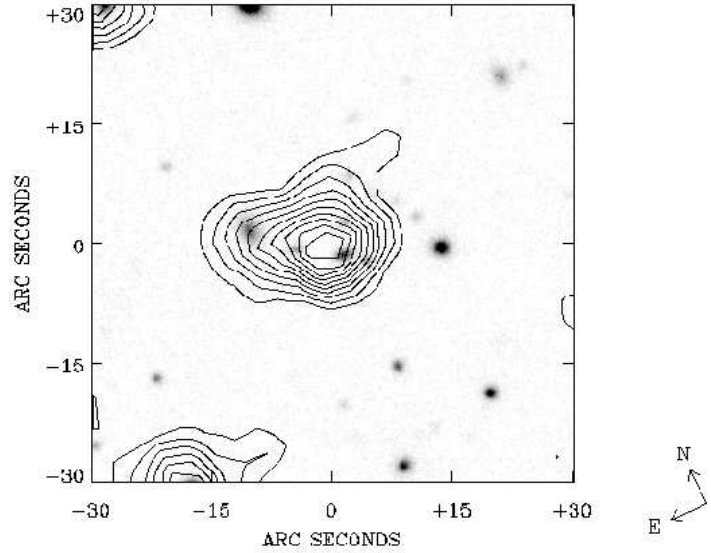


CENTER: R.A. 12 36 44.21 DEC 162 12 51.0 EQUINOX: J2000

Fig. 15. Comparison near-IR/LW3 filter for source HDF_PM_17. The contours of the details of the LW3 map around source 17 have been overlaid on the IRIM K map. Contour levels begin at $1.5 \mu\text{Jy}$ with steps of $2 \mu\text{Jy}$.

$5\tau_w$ upper limit as follows : a test image containing only the source is computed by projecting a point source as observed at each raster pointing in a copy of the final raster map. This ensures that the modification to the PSF produced by microscan are taken into account. The b-spline wavelet transform of this image is then calculated and compared to 5 times the noise map at each scale. The minimum flux ensuring the detection is then converted in microJansky, using our calibration from simulations.

All sources from the main list within the HDF have optical counterparts, thanks to the depth of the HST map,



CENTER: R.A. 12 36 49.79 DEC 162 13 15.0 EQUINOX: J2000

Fig. 16. Comparison near-IR/LW3 filter for source HDF_PM_27. The contours of the details of the LW3 map around source HDF_PM_27 have been overlaid on the IRIM K map. Contour levels begin at $1.5 \mu\text{Jy}$ with steps of $2 \mu\text{Jy}$.

but 6 sources within the flanking fields do not have visible counterparts in the much less deep F814W images. However, these 6 sources are very reliable and were also found by other teams (see below). The number of sources without counterpart rises to 11 in the supplementary list, of which 1 lays in the HDF. Source HDF_PS3_6e does not have any counterpart in the ‘iw’ HST image, but has a counterpart in the IRIM K image. This example shows that the reliability of the source should not be established on the existence of counterparts in optical images only, especially in the flanking fields. It is remarkable that all but one (3652+1444) of the radio sources observed at 8.4 GHz by Fomalont et al. (1997) in the field of view, are detected, mostly in the LW3 filter (Table 6), and one in the LW2 filter only (Table 5).

Other teams have used different algorithms to produce source lists. We have compared our results to those of the Imperial College group (hereafter IC) (Goldschmidt et al. 1997) and to those of IAS (Désert et al. 1998). The common source lists are given in Table 6 for the LW3 filter, and in Table 5 for the LW2 one, as well as the names of the radio sources observed at 8.4 GHz by Fomalont et al. (1997) matching ISOCAM sources.

PRETI and the “triple beam switch method” of IAS (Désert et al. 1998) give very similar results (see Table 5 and 6), especially in the LW3 band where out of the 41 sources detected by them, we find 37. We do not detect HDF_ALL_LW3_8,14,29,40 that are at 3.4σ , 3.3σ , 3.9σ and 3.1σ respectively, that is among the faintest of their list. Both number counts agrees above $200 \mu\text{Jy}$ where PRETI reaches 99.9% completeness : the two methods detect 24 sources. Figure 17 displays a comparison be-

tween the fluxes derived by the two methods for the common source list. The fluxes derived by the “triple beam switch method” are lower than our fluxes by a systematic factor of 0.82. We note that both methods rely on the ISOCAM cookbook values for the correction of ADUs into milli-Janskies. For one part, we can explain the difference by an implicit color correction that we have introduced in our simulations : our PSFs are simulated assuming a rising spectrum with spectral index of 3, while standard ISOCAM PSFs, used by Désert et al. 1998, are measured on stars, thus assuming a spectral index of (-2). When comparing our PSFs to standard ones, a mean difference of 10 % is found. Moreover, source fluxes are measured by us with aperture photometry while the “triple beam switch method” uses fits of gaussian of fixed width. Since at 6”, the ISOCAM PSF is only roughly approximated by a gaussian, this can account for the remaining discrepancy. At these faint level of fluxes, such differences are not very important, considering that the source lists of the two catalogues match very well. However, PRETI allows to reach deeper sensitivity, as we consider sources at 40 μJy as reliable. For the LW2 filter, the “triple beam switch method” detects 6 sources, 3 of which are also detected with PRETI. Of the 3 undetected objects, 2 lay on the edges of the map where we do not allow for detection. The last one is measured by Désert et al. at 58 μJy where we are not complete.

The IC group have made the original data reduction of the ISO-HDF, when some of the latest refinements of ISOCAM calibration such as field distortion were not available. We find 21 of the 22 sources detected by them in their LW3 image (Goldschmidt et al. 1997). We could not find the source J123659.4+621337 in our map. Source photometry differs from our catalog : on the average, their flux estimates are higher than ours by a factor of 1.5, as shown in figure 18. They performed simulations, and concluded that they should be 70% complete at a level of 225 μJy . According to the 1.5 factor of difference in photometry, they should have detected at least 26 of our 37 sources above 150 μJy , where they only find 19. This indicates that they are only 50% complete at this level, while PRETI reaches 95% at a level of 150 μJy , according to our simulations, if source confusion is ignored. Comparing the LW2 detections, we only find 5 of the 27 sources in their list (3 from their main list of 6 objects and 2 from their supplementary list of 21 objects), as shown in table 5. Moreover, we measure much fainter fluxes for these objects. Since this observation is made with 10s integration time, so that pixels affected by cosmic ray glitches are more numerous, two explanations can account for this : either we set too heavy a deglitching criterion and we have cleaned real sources out, or they did not clean their data enough against cosmic rays. Our analysis lead us to favor the second explanation, because we do not find that we are missing sources in the simulations. Here also the re-

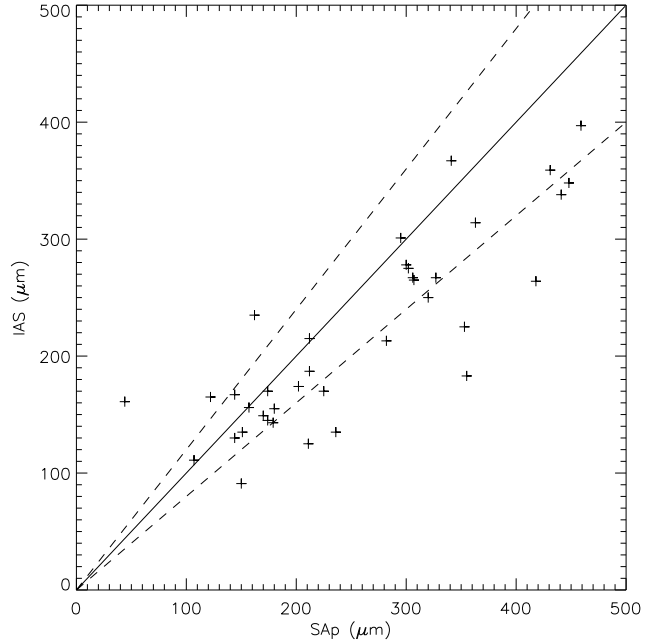


Fig. 17. Comparison of the photometry of common sources in the ISO-HDF at 15 μm for PRETI and IAS. Solid line is 1 to 1 relation, dashed lines are a 20 % error with respect to the 1 to 1 relation.

sults of Désert et al. (1998) are in good agreement with us.

6.3. Number counts

The small number of LW2 sources does not allow to compute reliable number counts, as the poissonian fluctuations introduce an uncertainty of plus or minus 40 % 1σ when using the reliable $7\tau_w$ source list. Nevertheless, we have, at the level of 100 μJy , 5 reliable detections in an area of $10.45'^2$, that is : $N(> 100\mu\text{Jy}) = 1.7 \times 10^3 \pm 8 \times 10^2$ sources per square degree, a value compatible with the prediction of a pure passive luminous evolution model of number counts (Franceschini et al. 1997), as shown on Fig. 19.

The more numerous detections in the LW3 band allow us to compute some points of the Log(N)-Log(S) curve, and to try to determine its slope. We determined two curves, using the $7\tau_w$ and $5\tau_w$ detection thresholds, for which a few more spurious detections are expected.

In order to compute reliable number counts, we have taken into account the following parameters :

1. the area available for detection at a given flux with a given detection threshold ($N\tau_w$) has been computed, using the same technique as for determining the upper limits of undetected sources. However, an additional hypothesis was made : each source is considered centered on a pixel of the map.

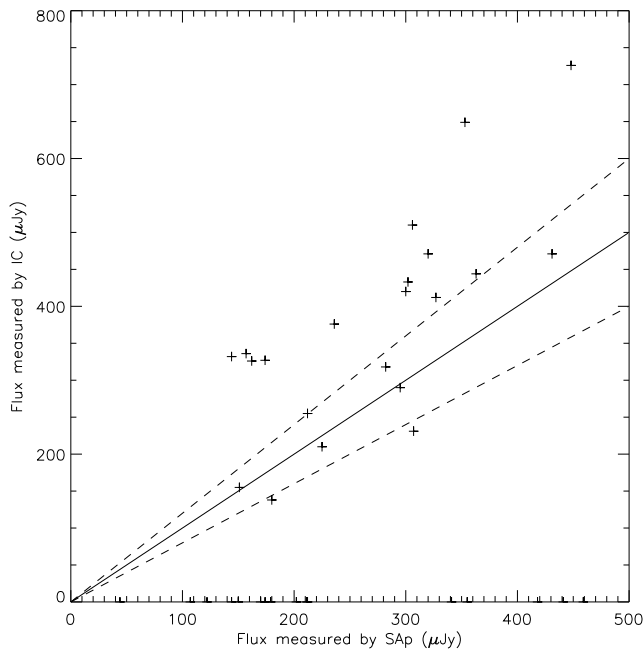


Fig. 18. Comparison of the photometry of common sources in the ISO-HDF at $15 \mu\text{m}$ for PRETI and IC. Solid line is 1 to 1 relation, dashed lines are a 20 % error with respect to the 1 to 1 relation

2. the blending of faint sources by bright ones is treated in a very simple way : the area occupied by the sources of all the brighter bins of flux is subtracted from the area available for the detection of sources at a given bin. For each source, we have taken out a circle of radius $9''$, that is approximately the distance between sources separated by PRETI.
3. we take the completeness of the detection at a given level into account by using the results of our simulations (see Fig. 6).
4. when dealing with the $5\tau_w$ detections, we have not taken source HDF_PS3_40 into account, because of its high probability of being a star.

This method leads us to derive the number counts that are plotted on Figs. 20 and 21, with error bars corresponding to 1σ poissonian fluctuations (as the square root of the number of events). Moreover, we have also plotted on these figure two extreme limits :

1. The ‘upper’ limit, where all sources are given their measured flux plus their positive error bar, to which we add the poissonian fluctuations.
2. The ‘lower’ lower, where all sources are given their measured flux minus their negative error bar, to which we subtract the poissonian fluctuations.

Finally, we have also plotted on these figures the prediction of a model with no evolution (Franceschini et al. 1997).

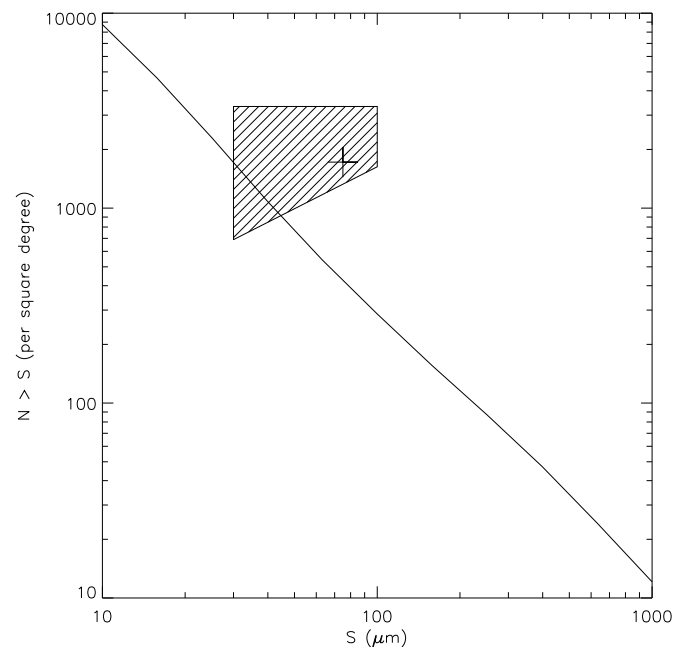


Fig. 19. Number counts in the ISO-HDF at $6.75 \mu\text{m}$, based on the $7\tau_w$ sample. Solid : no evolution model from Franceschini et al. (1997) Hatched area : 1σ error area for the integrated counts point (cross) from the $7\tau_w$ sample.

In both $7\tau_w$ and $5\tau_w$ sample, the straightforward result is that the counts derived from ISO-HDF in the LW3 band show a strong excess : nearly a factor of ten at $200 \mu\text{Jy}$, with respect to the prediction of the no evolution model. This excess is higher than the one obtained by Oliver et al. (1997) from the first reduction of the ISO-HDF data. This might be due to the underestimation of the completeness of the sample.

In order to test our simple method to account for blending, we have plotted in figure 21 the number counts obtained with the $5\tau_w$ sample with the method described when blending is not taken into account, but adding to our sample the unblended sources in our supplementary list. On this last plot, the slope of counts is constant down to $60 \mu\text{Jy}$, and slightly steeper than predicted in the framework of the no evolution model.

7. Discussion

The number counts derived from the ISO-HDF observations implying strong evolution at $15 \mu\text{m}$ and no evolution at $6.75 \mu\text{m}$, may appear surprising at first sight. This apparent discrepancy is in fact easy to interpret, considering that we are not observing the same physical processes at these two wavelengths.

As shown in Fig. 2, the LW2 filter tends to select the old stellar population of elliptical galaxies; taking advantage of the K correction, the detection of such systems

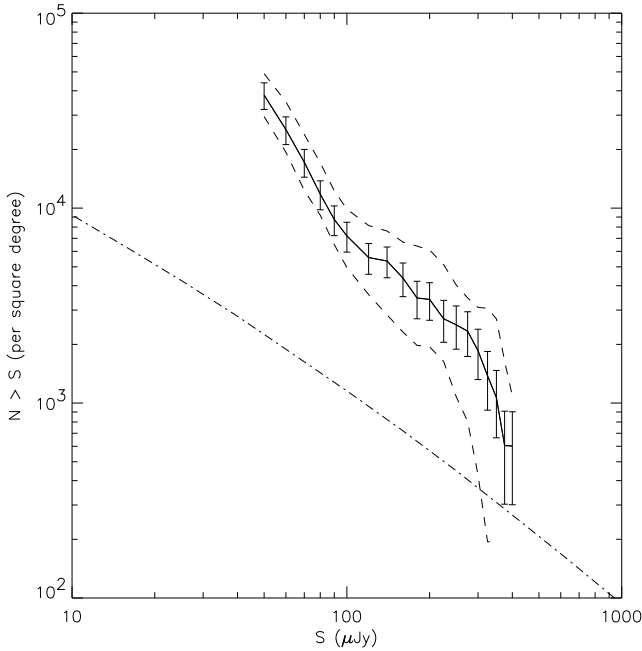


Fig. 20. Number counts in the ISO-HDF at $15 \mu\text{m}$, based on the $7\tau_w$ sample.

Solid : $7\tau_w$ with poissonian error bars.
dashed : ‘upper’ and ‘lower’ limits of counts.
dash-dotted : no evolution model

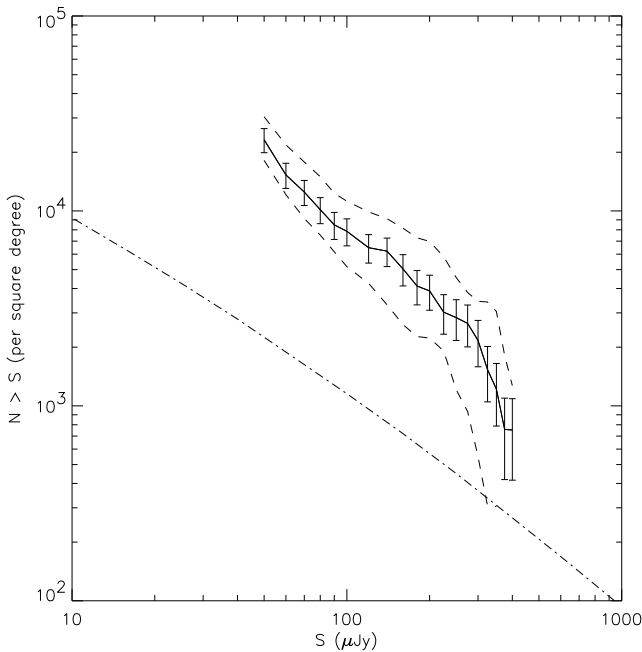


Fig. 21. Number counts in the ISO-HDF at $15 \mu\text{m}$, based on the $5\tau_w$ sample plus unblended sources.

Solid : $5\tau_w$ with poissonian error bars.
dashed : ‘upper’ and ‘lower’ limits of counts.
dash-dotted : no evolution model

are favored at $z > 0.5$. For gaseous systems, dominated by dust and UIB emission, as the redshift rises, the LW2 filter crosses a gap between the UIB features above $6.2 \mu\text{m}$ and stellar emission below $4 \mu\text{m}$ in the rest frame, leading to a small number of detections, even though the sensitivity is higher than with the LW3 filter.

The LW3 filter picks up hot dust in nearby systems as well as redshifted UIB emission at z as high as 1.5. Studies of nearby galaxies show that this emission is enhanced in the regions surrounding a starburst, so that the detection of starbursts, often in mergers, is favoured. This is borne out in the results. Indeed, a close examination of the morphology of ISO sources shows that early type galaxies are numerous among the few LW2 detections (6 out of 11 detections), while spirals, irregulars, or mergers dominate in the LW3 sample.

The z distribution of our sample of LW3 sources (with signal in wavespace 7 times above the threshold) is displayed in Fig. 22, and compared to that of sources with $B < 25$ and $K < 22$, taken from the list by Cowie et al. (1997). The redshifts in our sample range from $z = 0.078$ to $z = 1.242$, with a median value of $z = 0.585$; most of ISOCAM LW3 sources have $z > 0.4$. The distribution in redshift of our two samples is very similar, implying that the LW3 filter does not select a particular range in z .

A forthcoming paper (Elbaz et al., *in prep.*) will present a detailed study of each ISO-HDF sources. This study will allow to determine if the evolution observed at $15 \mu\text{m}$ is a general trend in galaxies or is due to certain types in the galaxy population, and put limits on the evolution of the early type systems at $z < 1.5$.

8. Conclusion

The PRETI method for faint source detection with ISOCAM has been successfully applied to the observation of the HDF and flanking fields. Faint fluxes are reached with a good reliability. Moreover, our simulations allow us to test the completeness and photometric accuracy of our results. On the ISO-HDF, the method gives a 99.9% completeness at $200 \mu\text{Jy}$ in LW3 when detecting above five times the noise level in wavelet space. The same completeness is obtained at $65 \mu\text{Jy}$ in LW2. Using PRETI, we detected 49 sources in our main source list, plus 51 in a less secure supplementary list. Most of the sources are detected at $15 \mu\text{m}$, 11 are detected at $6.7 \mu\text{m}$ only. Our results for the brightest sources are in good agreement with those of Désert et al. (1998) in both filters, as well as with those of Rowan-Robinson et al. (1997) at $15 \mu\text{m}$, but not at $6.75 \mu\text{m}$. The number counts derived for the LW3 filter show a clear excess of sources with respect to the predictions of a no evolution model (Franceschini et al. 1997). A forthcoming paper (Elbaz et al. *in prep.*) will refine these results with a source by source study and discuss extinction and star formation rates.

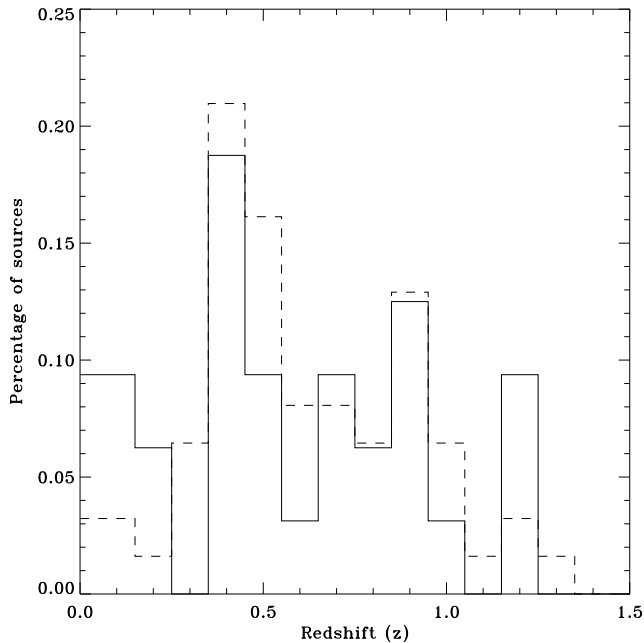


Fig. 22. Histogram of redshifts distribution in two samples

Solid : ISOCAM LW3 sources .

dashed : Cowie et al. (1997) sample on HDF with $B < 25$ and $K < 22$.

Acknowledgements. We wish to thank Alberto Franceschini for interesting discussions and comments along the preparation of this paper, as well as for having provided his models of number counts. We thank also François-Xavier Désert for useful discussions. We made use of the CAM Interactive Analysis Software (CIA), a joint development by the ESA Astrophysics Division and the ISOCAM Consortium. The ISOCAM Consortium is led by the ISOCAM PI, C. J. Cesarsky, Direction des Sciences de la Matière, C.E.A., France.

References

- Abergel, A., Bernard, J.-P., Boulanger, F., et al., 1996, A&A 315, L329
- Abraham, R. G., Tanvir, N. R., Santiago, B. X., et al., 1996, MNRAS 279, L47
- Aussel, H., ISOCAM LW channel field distortion, Technical report, Service d'Astrophysique, CEA/DSM/DAPNIA, CE-Saclay, Orme des Merisiers, F-91191 Gif-sur-Yvette cedex, France
- Aussel, H., Gerin M., Boulanger, F. et al., 1998, A&A 334, L73
- Bertin, E., Dennefeld, M., Moshir, M., A&A 323, 685
- Bressan, A., Granato, G. L., Silva, L., A&A 332, 135
- Cesarsky, C. J., Abergel, A., Agnès P. et al., 1996, A&A 315, L32
- Cesarsky, C. J., Elbaz, D., Les deep surveys ISOCAM. In : Examining the big bang and diffuse background radiations, Kafatos et al. (eds), IAU Symposium N. 168, p 106, Kluwer Academic publishers
- Cohen, J. G., Cowie, L. L., Hogg, D. W., et al., 1996, ApJ 471, L5
- Colley, W. N., Rhoads, J. E., Ostriker, J. P., et al., 1996, ApJ 473, L63
- Connolly, A. J., Szalay, A. S., Dickinson, M., et al., 1997, ApJ 486, L11
- Cowie, L. L., Songaila-Cowie, A., 1997, Hawaii Active Catalog, Institute for Astronomy, University of Hawaii, <http://www.ifa.hawaii.edu/~cowie/tts/tts.html>
- Désert, F.-X., Boulanger, F., Puget, J.-L., 1990, A&A 237, 215
- Désert, F.-X., Puget, J.-L., Clements, D. L., et al., A&A in press
- Dickinson M. et al., 1997, in prep
- Elbaz., D., Aussel., H., Cesarsky C. J., 1998, in prep
- Ellis, R. S., 1997, ARA&A 35, 389
- Fomalont, E. B., Kellermann, K. I., Richards, E. A. et al., 1997, ApJ 475, L5
- Franceschini, A., 1998, The extragalactic Infrared Background. In : Extragalactic Astronomy in the Infrared, Mamon G. A., Thuan T. X., Tran Thanh Van J. (eds), Moriond Series in Astrophysic, p 509, Editions Frontieres
- Franceschini, A., Aussel, H., Bressan, A., 1997, Source Counts and Background Radiation. In : The Far Infrared and Submillimeter Universe, ESA FIRST Symposium (ESA SP 401). preprint : astro-ph/9707080
- Franceschini, A., de Zotti, G., Toffolatti, L., et al., 1991, A&AS 89, 285
- Goldschmidt, P., Oliver, S. J., Serjeant, S. B. G. et al., 1997, MNRAS 289, 465
- Gregorich, D. T., Neugebauer, G., Soifer, B. T., et al., 1995, AJ 110, 259
- Helou G., Soifer, B. T., Rowan-Robinson, M., 1985, ApJ 298, L7
- Hibbard, J. E., Vacca, W. D., 1997, AJ 114, 1741
- Hogg, D. W., Neugebauer, G., Armus, L. et al., 1997a, AJ 113, 474
- Hogg, D. W., Cohen, J. G., Blandford, R., et al., 1997b, AJ 115, 1418
- Holtzman, J. A., Burrows, C. J., Casertano, S., et al., 1995, PASP 107, 1065
- Kessler, M. F., Steinz, J. A., Anderegg, M. E., et al., 1996, A&A 315, L27
- Lilly, S. J., Lefevre, O., Hammer, F., et al., 1996, ApJ 460, L1
- Madau, P., Fergusson, H. C., Dickinson, M. E., et al., MNRAS 283, 67
- Madden, S. C., Vigroux, L., Sauvage, M., 1998, Mid Infrared Observations of early-types galaxies. In : Extragalactic Astronomy in the Infrared, Mamon G. A., Thuan T. X., Tran Thanh Van J. (eds), Moriond Series in Astrophysic, p 509, Editions Frontieres
- Mann, R. G., Oliver, S. J., Serjeant, S. B. G., et al., 1997, MNRAS 289, 482
- Maoz, D., 1996, ApJ 490, L135
- Meurer, G. R., Heckman, T. M., Lehnert, M. D. et al., 1997, AJ 114, 54
- Moorwood, A. F. M., Lutz, D., Oliva, E., et al., A&A 315, L109
- Okumura, K., 1997, ISOCAM PSF Report, ESA/CAM IDT, http://isowww.estec.esa.nl:80/instr/CAM/cal_wksp/
- Oliver, S. J., Goldschmidt, P., Franceschini, A., et al., 1997, MNRAS 289, 471
- Phillips, A. C., Guzman, R., Gallego, J., et al., 1997, ApJ 489, 543

- Richards E. C., Kellerman, K. I., Fomalont, E. B., 1997, Radio observation of the Hubble Deep Field, NRAO Repr. Ser. A
- Rowan-Robinson, M., Mann, R. G., Oliver, S. J., et al., 1997, MNRAS 289, 490
- Serjeant, S. B. G., Eaton, N., Oliver, S. J., et al., 1997, MNRAS 289, 457
- Starck, J.-L., Aussel, H., Elbaz, D. and others, 1998, Faint Source Detection with ISOCAM using the PRETI method, In : Extragalactic Astronomy in the Infrared, Mamon G. A., Thuan T. X., Tran Thanh Van J. (eds), Moriond Series in Astrophysics, p 509, Editions Frontieres
- Steidel, C. C., Giavalisco, M., Dickinson, M., et al., 1996, AJ 112, 352
- Taniguchi, Y., Cowie, L. L., Sato, Y., et al., 1997, A&A 237, L9
- Tran, Q. D., 1998, Emission du milieu interstellaire local et extragalactique dans l'infrarouge moyen : l'apport d'ISOCAM, PhD Thesis, Université de Paris XI, Orsay, France
- Williams, R. E., Blacker, B., Dickinson, M., et al., 1996, AJ 112, 1335

Table 4. PRETI supplementary source list for the ISOHDF observations at $6.5\mu\text{m}$ (LW2) and $15\mu\text{m}$ (LW3). All LW3 sources are at least detected at $3\tau_w$ above readout and photon noise, while all LW2 sources are detected atleast above $5\tau_w$. (1) : Source identification ‘PS3’ is for PRETI supplementary list LW3 and ‘PS2’ for LW2. Sources with letter at the end, like ‘6a’ are deblended neighbours of the source with same number in the main list. (2),(3) : source position for the J2000.0 equinox. (4) : source flux in microJansky in the LW2 filter with error bar or upper limit ($5\tau_w$). A ‘-’ indicates that the source is not in the LW2 field. (5) : source flux in ADU/G/s in a $3''$ aperture. (6) : detection level ($n\tau_w$) in the LW2 image.(7) : source flux in microJansky in the LW3 filter with error bar or upper limit ($5\tau_w$). (8) : source flux in ADU/G/s in a $6''$ aperture. (9) : detection level ($n\tau_w$) in the LW3 image. (10) : Identifier of the HST field in which the source falls (hd stands for HDF, others for flanking fields, ‘-’ means outside of all HST fields). (11) : spectroscopic redshift with source incated by a note. (c) : data from Cohen et al. (1996), (p) : data from Phillips et al. (1997), (i) : compiled in Cowie et al. (1997), (h) data from Hogg et al. (1977b). (12) : morphological type of the object. ‘(i)’ indicates a type compiled in Cowie et al. (1997), ‘(p)’ type from Phillips et al. (1997), otherwise determined by us. E : Elliptical or S0 galaxy. S : spiral. M : merger. P : peculiar/irregular, C : compact object from Phillips et al. (1997) sample, A : active nuclei galaxy, G : source falls on a group. U : unknown type. N : no optical counterpart. K : counterpart only in IRIM K image. st : star-like object . A ‘?’ indicates a dubious type identification.

Id ⁽¹⁾	α ⁽²⁾ (J2000)	δ ⁽³⁾ (J2000)	LW2 ⁽⁴⁾ μJy	LW2 ⁽⁵⁾ ADU/G/s	$N\tau_w$ (6)	LW3 ⁽⁷⁾ μJy	LW3 ⁽⁸⁾ ADU/G/s	$N\tau_w$ (9)	F (10)	z ⁽¹¹⁾	T ⁽¹²⁾
HDF_PS3_1	12 36 30.5	+62 12 09	-	-	-	145 ⁺⁷³ ₋₄₈	0.085	3	sw	0.456 ^(c)	E?
HDF_PS3_2	12 36 32.2	+62 11 33	-	-	-	44 ⁺²⁸ ₋₀₉	0.035	4	sw	-	N
HDF_PS3_3	12 36 33.5	+62 13 21	-	-	-	122 ⁺⁵⁴ ₋₄₀	0.069	4	iw	0.843 ^(c)	P
HDF_PS3_4	12 36 33.9	+62 14 03	-	-	-	174 ⁺⁵⁹ ₋₄₃	0.099	3	iw	-	U
HDF_PS3_5	12 36 36.5	+62 14 48	-	-	-	44 ⁺³⁰ ₋₀₉	0.035	4	iw	-	N
HDF_PS3_6a	12 36 36.9	+62 13 36	-	-	-	184 ⁺⁶¹ ₋₄₄	0.105	-	iw	-	P
HDF_PS3_7	12 36 38.2	+62 14 33	-	-	-	29 ⁺¹¹ ₋₁₃	0.026	3	iw	-	N
HDF_PS3_8	12 36 38.6	+62 14 51	-	-	-	52 ⁺³⁴ ₋₀₉	0.042	-	nw	-	N
HDF_PS3_6b	12 36 38.7	+62 13 39	-	-	-	52 ⁺³⁴ ₋₉	0.042	-	iw	-	U
HDF_PS3_11a	12 36 39.1	+62 12 57	< 90	-	-	211 ⁺⁵⁸ ₋₅₄	0.119	-	iw	-	S
HDF_PS3_6c	12 36 40.4	+62 13 36	-	-	-	36 ⁺¹¹ ₋₁₅	0.029	-	iw	-	U
HDF_PS3_6d	12 36 40.4	+62 13 45	-	-	-	24 ⁺¹⁰ ₋₁₂	0.020	3	iw	-	N
HDF_PS3_9	12 36 40.8	+62 10 48	-	-	-	44 ⁺³⁰ ₋₀₉	0.035	3	sw	-	N
HDF_PS3_6e	12 36 41.9	+62 13 33	-	-	-	23 ⁺¹⁰ ₋₁₂	0.019	4	iw	-	K
HDF_PS3_10	12 36 42.1	+62 15 45	-	-	-	459 ⁺⁴⁶ ₋₈₆	0.263	6	-	-	-
HDF_PS3_12	12 36 43.0	+62 10 51	-	-	-	18 ⁺⁹ ₋₁₀	0.014	-	sw	-	N
HDF_PS3_21a	12 36 43.4	+62 11 51	< 41	-	-	48 ⁺⁵⁷ ₋₁₀	0.044	-	hd	1.242 ⁽ⁱ⁾	U ⁽ⁱ⁾
HDF_PS3_13	12 36 43.4	+62 14 30	< 405	-	-	6 ⁺⁸ ₋₇	0.005	-	nw	-	N
HDF_PS3_21c	12 36 44.7	+62 11 51	< 41	-	-	111 ⁺⁵² ₋₃₈	0.063	-	hd	2.803 ⁽ⁱ⁾	M ⁽ⁱ⁾
HDF_PS3_17b	12 36 44.7	+62 13 03	< 60	-	-	33 ⁺¹¹ ₋₁₅	0.027	-	hd	0.485 ^(p)	S
HDF_PS3_21b	12 36 45.1	+62 11 42	< 47	-	-	147 ⁺⁷³ ₋₄₈	0.086	-	hd	-	C ⁽ⁱ⁾
HDF_PS2_1	12 36 45.4	+62 12 39	77 ⁺⁶⁷ ₋₆₆	0.009	5	< 74	-	-	hd	-	S ⁽ⁱ⁾
HDF_PS3_17a	12 36 45.9	+62 12 45	< 47	-	-	31 ⁺¹¹ ₋₁₄	0.025	-	hd	-	E ⁽ⁱ⁾
HDF_PS2_2	12 36 46.2	+62 11 46	88 ⁺⁴⁵ ₋₅₀	0.009	5	< 78	-	-	hd	0.504 ^(c)	E ⁽ⁱ⁾
HDF_PS3_14	12 36 47.7	+62 10 21	-	-	-	104 ⁺⁹⁴ ₋₂₁	0.075	3	se	-	N
HDF_PS2_3	12 36 47.7	+62 13 12	36 ⁺⁶⁵ ₋₃₀	0.003	5	< 74	-	-	hd	0.475 ^(c)	E
HDF_PS3_15	12 36 48.9	+62 12 18	-	-	-	32 ⁺¹¹ ₋₁₄	0.025	4	hd	0.953 ^(p)	M ⁽ⁱ⁾
HDF_PS3_16	12 36 50.2	+62 12 39	< 34	-	-	22 ⁺¹⁰ ₋₁₁	0.018	4	hd	0.474 ^(c)	M ⁽ⁱ⁾
HDF_PS3_18	12 36 51.9	+62 10 24	-	-	-	118 ⁺⁵³ ₋₃₉	0.067	5	se	-	P
HDF_PS3_19	12 36 51.9	+62 11 48	-	-	-	34 ⁺¹¹ ₋₁₅	0.027	4	se	-	N
HDF_PS3_30a	12 36 52.0	+62 14 00	< 39	-	-	50 ⁺⁷⁹ ₋₂₀	0.040	-	hd	0.557 ⁽ⁱ⁾	S? ⁽ⁱ⁾
HDF_PS3_20	12 36 52.8	+62 14 54	-	-	-	42 ⁺²⁹ ₋₉	0.033	3	nw	0.463 ^(c)	M
HDF_PS3_22	12 36 54.1	+62 14 36	< 136	-	-	51 ⁺⁷⁵ ₋₅₁	0.047	5	ne	0.577 ^(c)	U
HDF_PS3_23	12 36 54.9	+62 11 27	-	-	-	42 ⁺²⁹ ₋₀₉	0.032	3	ie	-	U
HDF_PS3_24	12 36 55.4	+62 13 12	< 37	-	-	23 ⁺¹⁰ ₋₁₁	0.018	3	hd	1.315 ^(h)	E ⁽ⁱ⁾
HDF_PS3_25	12 36 55.5	+62 15 15	-	-	-	75 ⁺⁷¹ ₋₁₉	0.052	3	nw	-	N
HDF_PS3_26	12 36 55.8	+62 12 45	< 38	-	-	44 ⁺⁷⁰ ₋₀₉	0.035	5	hd	0.790 ^(c)	S? ⁽ⁱ⁾
HDF_PS3_27	12 36 56.2	+62 11 33	-	-	-	29 ⁺¹¹ ₋₁₃	0.023	3	ie	-	N
HDF_PS2_4	12 36 56.7	+62 13 03	94 ⁺⁵⁰ ₋₆₉	0.012	6	< 54	-	-	hd	-	E ⁽ⁱ⁾

Continued on next page...

Continued from previous page...

Id ⁽¹⁾	$\alpha^{(2)}$ (J2000)	$\delta^{(3)}$ (J2000)	LW2 ⁽⁴⁾ μJy	LW2 ⁽⁵⁾ ADU/G/s	$N\tau_w$ (6)	LW3 ⁽⁷⁾ μJy	LW3 ⁽⁸⁾ ADU/G/s	$N\tau_w$ (9)	F (10)	$z^{(11)}$	T ⁽¹²⁾
HDF_PS3_28	12 36 56.7	+62 13 30	< 50	-	-	26^{+10}_{-13}	0.021	4	hd	-	N
HDF_PS3_29	12 36 58.8	+62 11 18	-	-	-	9^{+8}_{-7}	0.007	4	ie	-	U
HDF_PS3_31	12 37 00.1	+62 11 54	< 150	-	-	48^{+56}_{-10}	0.045	6	ie	-	G
HDF_PS3_32	12 37 01.8	+62 11 45	-	-	-	15^{+9}_{-9}	0.012	3	ie	-	S?
HDF_PS3_33	12 37 01.8	+62 14 39	-	-	-	21^{+10}_{-11}	0.017	3	ne	-	N
HDF_PS3_34	12 37 02.7	+62 12 48	< 322	-	-	44^{+30}_{-9}	0.035	4	ie	-	E?
HDF_PS3_35	12 37 03.4	+62 13 51	-	-	-	29^{+11}_{-13}	0.023	3	ie	-	N
HDF_PS3_36	12 37 04.4	+62 14 48	-	-	-	80^{+74}_{-19}	0.056	3	ie	-	N
HDF_PS3_37	12 37 04.8	+62 14 27	-	-	-	72^{+65}_{-16}	0.050	3	ie	0.561 ^(c)	S
HDF_PS3_38	12 37 08.2	+62 12 48	-	-	-	89^{+79}_{-20}	0.061	6	ie	0.654 ^(p)	S?
HDF_PS3_39	12 37 08.2	+62 12 54	-	-	-	115^{+53}_{-39}	0.066	6	ie	0.838 ^(c)	P
HDF_PS3_40	12 37 09.5	+62 12 36	-	-	-	306^{+62}_{-67}	0.178	6	ie	-	st

Table 5. Comparison of the LW2 catalog obtained here with PRETI, with the catalogs by IC (Goldschmidt et al. 1997) and IAS (Désert et al. 1998), as well as radio sources detected at 8.4 GHz (Fomalont et al. 1997)

ID	Flux	IC	Flux	IAS	Flux	8.4 GHz	Flux
HDF_PM2_1	127^{+99}_{-61}	J123641.6+621142	51.6	-	-	-	-
HDF_PM2_2	185^{+99}_{-25}	-	-	-	-	3644+1133	458
HDF_PM3_20	191^{+41}_{-86}	J123646.4+621406	52.1	HDF-2_LW2_1	69.	3646+1404	152
HDF_PM3_24	254^{+71}_{-73}	J123648.2+621427	65.7	HDF-2_LW2_2	96.	-	-
HDF_PM2_3	41^{+66}_{-30}	-	-	HDF-2_LW2_3	48.	-	-
HDF_PM3_27	136^{+68}_{-57}	J123649.7+621315	48.1	-	-	3649+1313	22
HDF_PS2_4	94^{+50}_{-69}	J123656.6+621307	31.3	-	-	-	-

Table 6. Comparison of the LW3 catalog obtained here with PRETI, with the catalogs by IC (Goldschmidt et al. 1997) and IAS (Désert et al. 1998), as well as radio sources detected at 8.4 GHz (Fomalont et al. 1997)

ID	Flux	IC	Flux	IAS	Flux	8.4 GHz	Flux
HDF_PM3_1	355 ⁺⁴⁰ ₋₆₀	-	-	HDF_ALL_LW3_1	183	-	-
HDF_PM3_2	448 ⁺⁶⁸ ₋₅₉	J123633.9+621217	726	HDF_ALL_LW3_3	348	3634+1212	40
HDF_PS3_3	122 ⁺⁵⁴ ₋₄₀	-	-	HDF_ALL_LW3_2	165	-	-
HDF_PS3_4	174 ⁺⁵⁹ ₋₄₃	-	-	HDF_ALL_LW3_5	145	-	-
HDF_PM3_3	363 ⁺⁷⁹ ₋₃₈	J123634.3+621238	444	HDF_ALL_LW3_4	314	3634+1240	40
HDF_PM3_5	441 ⁺⁴³ ₋₃₂	-	-	HDF_ALL_LW3_6	338	-	-
HDF_PM3_6	353 ⁺⁴⁰ ₋₆₆	J123636.5+621348	649	HDF_ALL_LW3_10	225	-	-
HDF_PS3_6e	23 ⁺¹⁰ ₋₁₂	-	-	-	-	3642+1331	80
HDF_PM3_7	300 ⁺⁶² ₋₆₇	J123635.9+621134	420	HDF_ALL_LW3_7	278	-	-
HDF_PM3_8	202 ⁺⁵⁸ ₋₅₀	-	-	HDF_ALL_LW3_9	174	-	-
HDF_PM3_9	212 ⁺⁵⁸ ₋₅₅	J123637.5+621109	255	HDF_ALL_LW3_12	215	-	-
HDF_PM3_10	212 ⁺⁵⁸ ₋₅₂	-	-	HDF_ALL_LW3_11	187	-	-
HDF_PM3_11	302 ⁺⁵⁷ ₋₅₅	J123639.3+621250	433	HDF_ALL_LW3_15	275	-	-
HDF_PS3_11a	211 ⁺⁵⁸ ₋₅₄	-	-	HDF_ALL_LW3_13	125	-	-
HDF_PM3_12	236 ⁺⁶¹ ₋₅₈	J123641.1+621129	376	HDF_ALL_LW3_17	135	-	-
HDF_PS3_9	44 ⁺³⁰ ₋₀₉	-	-	HDF_ALL_LW3_16	161	-	-
HDF_PS3_10	459 ⁺⁴⁶ ₋₈₆	-	-	HDF_ALL_LW3_18	397	-	-
HDF_PM3_17	282 ⁺⁶⁰ ₋₆₄	J123643.7+621255	318	HDF_ALL_LW3_19	213	3644+1249	13
HDF_PM3_19	170 ⁺⁵⁹ ₋₄₂	-	-	HDF_ALL_LW3_20	149	-	-
HDF_PM3_20	107 ⁺⁹⁵ ₋₂₀	-	-	HDF_ALL_LW3_21	111	3646+1404	152
HDF_PM3_21	418 ⁺⁹¹ ₋₉₄	-	-	HDF_ALL_LW3_22	264	-	-
HDF_PM3_22	327 ⁺³⁹ ₋₆₃	J123646.9+621045	412	HDF_ALL_LW3_23	267	-	-
HDF_PM3_23	144 ⁺⁷² ₋₄₇	-	-	HDF_ALL_LW3_24	130	3646+1448	36
HDF_PM3_24	307 ⁺⁶² ₋₆₇	J123648.1+621432	231	HDF_ALL_LW3_25	265	-	-
HDF_PM3_26	150 ⁺⁷⁴ ₋₄₈	-	-	HDF_ALL_LW3_26	91	-	-
HDF_PM3_27	320 ⁺³⁹ ₋₆₂	J123649.8+621319	471	HDF_ALL_LW3_27	250	3649+1313	22
HDF_PM3_28	341 ⁺⁴⁰ ₋₆₅	-	-	HDF_ALL_LW3_28	367	-	-
HDF_PM3_29	48 ⁺³² ₋₀₉	-	-	-	-	3651+1221	18
HDF_PM3_30	151 ⁺⁷⁴ ₋₆₈	J123651.5+621357S	155	HDF_ALL_LW3_30	135	-	-
HDF_PM3_31	174 ⁺⁵⁹ ₋₄₃	J123653.0+621116	327	HDF_ALL_LW3_31	170	-	-
HDF_PM3_32	180 ⁺⁶⁰ ₋₄₃	J123653.6+621140	138	HDF_ALL_LW3_32	155	3653+1139	15
HDF_PM3_33	179 ⁺⁶⁰ ₋₄₃	-	-	HDF_ALL_LW3_33	143	-	-
HDF_PS3_24	23 ⁺¹⁰ ₋₁₁	-	-	-	-	3655+1311	12
HDF_PS3_37	225 ⁺⁶⁰ ₋₅₆	J123658.1+621458S	210	HDF_ALL_LW3_34	170	-	-
HDF_PS3_39	157 ⁺⁷⁵ ₋₄₉	J123658.7+621212	336	HDF_ALL_LW3_35	156	-	-
HDF_PS3_40	295 ⁺⁶¹ ₋₆₆	J123700.2+621455	290	HDF_ALL_LW3_36	301	-	-
HDF_PS3_32	15 ⁺⁹ ₋₉	-	-	-	-	3701+1147	19
HDF_PM3_42	162 ⁺⁷⁶ ₋₄₉	J123702.0+621127	326	HDF_ALL_LW3_37	235	-	-
HDF_PM3_44	144 ⁺⁷³ ₋₄₇	J123702.5+621406	332	HDF_ALL_LW3_38	167	-	-
HDF_PM3_45	431 ⁺⁴³ ₋₈₀	J123705.7+621157	471	HDF_ALL_LW3_39	359	-	-
HDF_PS3_40	306 ⁺⁶² ₋₆₇	J123709.8+621239	510	HDF_ALL_LW3_41	267	-	-
HDF_PS3_38	89 ⁺⁷⁹ ₋₂₀	-	-	-	-	3708+1245	15